



## Article

# Robust metal–organic framework with multiple traps for trace Xe/Kr separation

Huiping Zhang<sup>a</sup>, Yaling Fan<sup>a</sup>, Rajamani Krishna<sup>b</sup>, Xuefeng Feng<sup>a</sup>, Li Wang<sup>a</sup>, Feng Luo<sup>a,\*</sup>

<sup>a</sup>School of Biology, Chemistry and Material Science, East China University of Technology, Nanchang 344000, China

<sup>b</sup>Van't Hoff Institute for Molecular Sciences, University of Amsterdam, 1098 XH Amsterdam, the Netherlands

## ARTICLE INFO

## Article history:

Received 3 November 2020

Received in revised form 10 December 2020

Accepted 21 December 2020

Available online 29 December 2020

## Keywords:

Xe/Kr separation

MOFs

UNF off-gas

Multiple traps

## ABSTRACT

Direct separation of Xe and Kr from air or used nuclear fuel (UNF) off-gas by means of porous adsorbents is of industrial importance but is a very challenging task. In this work, we show a robust metal–organic framework (MOF), namely ECUT-60, which renders not only high chemical stability, but also unique structure with multiple traps. This leads to the ultrahigh Xe adsorption capacity, exceeding most reported porous materials. Impressively, this MOF also enables high selectivity of Xe over Kr, CO<sub>2</sub>, O<sub>2</sub>, and N<sub>2</sub>, leading to the high-performance separation for trace quantities of Xe/Kr from a simulated UNF reprocessing off-gas. The separation capability has been demonstrated by using dynamic breakthrough experiments, giving the record Xe uptake up to 70.4 mmol/kg and the production of 19.7 mmol/kg pure Xe. Consequently, ECUT-60 has promising potential in direct production of Xe from UNF off-gas or air. The separation mechanism, as unveiled by theoretical calculation, is attributed to the multiple traps in ECUT-60 that affords rigid restrict for Xe atom via van der Waals force.

© 2020 Science China Press. Published by Elsevier B.V. and Science China Press. All rights reserved.

## 1. Introduction

Xenon and krypton are gaseous fine chemical products, called as “gold gas”, due to their broad applications in lighting, flat screen TV, electronic chip, hollow glass, space, satellite, medical, and scientific research [1]. At present the commercial price of xenon is up to RMB 120,000 per cubic meter in China. The global demand of Xe and Kr in 2010 is up to 11 and 93 millions litres, respectively ([http://www.qiti88.com/dynamic/gcgcxq\\_1.html](http://www.qiti88.com/dynamic/gcgcxq_1.html)).

There are two major sources of Xe and Kr. Firstly, recovery from ambient air that contains 0.087 ppmv (Xe) and 1 ppmv (Kr). The recovery from ambient air requires expensive large-scale air separation equipment and suffers the possibility of explosion hazard during condensing process with excessive CH<sub>4</sub> [2,3]. Secondly, Xe and Kr are recoverable from the off-gases from used nuclear fuel (UNF), containing 400 ppm Xe and 40 ppm Kr [4].

The currently used technology for production of Xe and Kr is cryogenic distillation. However, this is highly energy-intensive. Alternatively, adsorption based separation could be a good candidate. But the traditional porous materials such as zeolite and porous carbon are not viable adsorbents, due to their small Xe adsorption capacity and low Xe adsorption selectivity [5]. Some

porous organic porous materials have been shown selective adsorption of Xe over Kr, but these adsorbents often have low adsorption capacity or weak selectivity, as well as weak thermal and chemical stability [6].

Metal–organic frameworks (MOFs) [7,8] present a promising porous platform, built on metal ions and various organic ligands, showing high porosity, molecular designability, abundance inner surrounding of pore, and so on [9–11]. This category has been extensively explored for separation covering alkyne/alkene, alkene/alkane, isomer, and isotope separation [12–17]. Several MOFs also enable outstanding Xe/Kr separation [18–26]. For example, ZU-62 reported by Xing and co-workers [18] affords ultrahigh Xe/Kr uptake ratio up to 43.29 at low pressure and 273 K, due to a open-gating behavior, leading to benchmark Kr productivity of 206 mL/g and Xe productivity (42 mL/g) from a 20:80 (v:v) Xe/Kr mixture, similar to the byproduct after cryogenic air separation. In another case, Li et al. [26] reported a squarate-based MOF with exactly matchable size for Xe, resulting in the record Xe/Kr selectivity up to 60.6 at low pressure. Notably, in some reports the direct Xe/Kr separation from trace Xe/Kr mixture were proposed. For example, the Xe/Kr separation ability for SBMOF-1 [25], Ni-MOF-74 [27], CC3 [10], and the squarate-based MOF [26] was evaluated from the simulated UNF reprocessing off-gas (400 ppm Xe vs. 40 ppm Kr). However, their low Xe uptake under this extreme condition, such as 13.2 mmol/kg for SBMOF-1, 11 mmol/kg for

\* Corresponding author.

E-mail address: [ecitluofeng@163.com](mailto:ecitluofeng@163.com) (F. Luo).

CC3, and 4.8 mmol/kg for Ni-MOF-74, still could not meet the practical demand for direct production of Xe from UNF off-gas or air.

In this work, we present a robust MOF (ECUT-60) that enables ultrahigh Xe adsorption capacity at room temperature. Remarkably, this MOF also performs unprecedented separation performance for trace Xe/Kr through dynamic breakthrough experiments, leading to record Xe uptake up to 70.4 mmol/kg and the production of 19.7 mmol/kg pure Xe. Further insights into the separation mechanism was revealed by both the grand canonical Monte Carlo (GCMC) simulations and density functional theory (DFT-D) calculations.

## 2. Experimental

### 2.1. Materials

$\text{Co}(\text{NO}_3)_2 \cdot 6\text{H}_2\text{O}$ , 1,2-bis(4-pyridyl)ethylene, olsalazine sodium, and *N,N*-dimethylformamide (DMF) in analytical grade are purchased from innochem and used without any further purification.

### 2.2. Synthesis of ECUT-60

$\text{Co}(\text{NO}_3)_2 \cdot 6\text{H}_2\text{O}$  (0.1 mmol, 29.1 mg), 1,2-bis(4-pyridyl)ethylene (0.1 mmol, 18.2 mg) and olsalazine sodium (0.1 mmol, 34.62 mg) were dissolved in a mixture of 3 mL  $\text{H}_2\text{O}$  and 5 mL *N,N*-dimethylformamide. The solution was moved into a 25 mL Teflon-lined stainless steel vessel and heated at 115 °C for 3 d. Then it is cooled down to room temperature. Red crystals were filtered and washed with 10 mL ethanol and 10 mL deionized water. The yield was 81% based on Co(II). The experimental element analysis (%) is C/56.23, N/11.53, H/3.66.

### 2.3. Instrumentation

The optical images were accepted from Optec SZ810 microscope. Thermogravimetric analysis (TG) was performed by a TGA Q500 under a  $\text{N}_2$  atmosphere from room temperature to 800 °C at a rate of 10 °C/min. The data of X-ray powder diffraction were collected on a Bruker AXSD8 Discover powder diffractometer at 40 kV/40 mA for Cu  $\text{K}\alpha$  ( $\lambda = 1.5406 \text{ \AA}$ ) at room temperature in the range of 5°–50° ( $2\theta$ ) with a scan speed of 0.1° per step. The gas adsorption isotherms were collected on a Belsorp-max. The gases  $\text{N}_2$ ,  $\text{O}_2$ ,  $\text{CO}_2$ ,  $\text{C}_2\text{H}_2$ , and  $\text{C}_2\text{H}_4$ , Xe and Kr gases were used in this adsorption experiment were ultrahigh-purity-grade (>99.999%).

## 3. Results and discussion

Red crystals of ECUT-60 ( $\text{Co}_2(\text{bpe})(\text{OLZ}^{4-})$ , bpe = 1,2-bis(4-pyridyl)ethylene,  $\text{OLZ}^{4-}$  = olsalazine) were obtained by the solvothermal reaction of bpe,  $\text{Na}_2\text{H}_2\text{OLZ}$ , and  $\text{Co}(\text{NO}_3)_2 \cdot 6\text{H}_2\text{O}$  at 115 °C for 3 d. The yield is 81% and the purity was confirmed by powder X-ray diffraction (PXRD, Fig. S1 online). Single crystal XRD reveals that ECUT-60 crystallizes in the monoclinic system with space group  $\text{C}2/c$  and the asymmetric unit contains of one bpe ligand, a half of deprotonated  $\text{OLZ}^{4-}$  ligand, two Co(II) centers with site occupation of 0.5, and one coordinated water molecule with site occupation of 0.5. Co1 site adopts a seven-coordinated pentagonal bipyramid geometry finished by four oxygen atoms from two  $\text{OLZ}^{4-}$  carboxyl groups, two bpe nitrogen atoms, and one terminal coordinated water molecule. Whereas a regular octahedral geometry is observed for Co2 site, where the coordination atoms are composed of two oxygen atoms from two  $\text{OLZ}^{4-}$  carboxyl groups, two oxygen atoms from two  $\text{OLZ}^{4-}$  deprotonated hydroxyl groups, and two bpe nitrogen atoms. The completely deprotonated  $\text{OLZ}^{4-}$

ligands show the  $\mu_4:\eta^1:\eta^2:\eta^1:\eta^1:\eta^2:\eta^1$  coordination mode, while the bpe ligands afford the common bridging fashion to bind with two Co(II) ions (Fig. 1a). Along crystallographic *c*-axis the metal ions are connected by  $\text{OLZ}^{4-}$  ligands through one carboxylate oxygen bridge, constructing the rod-like building blocks (Fig. 1b and c). Further each rod subunit connects to six identical rod counterparts through both  $\text{OLZ}^{4-}$  skeleton and bpe linkers, creating the overall structure with hex-type [22] rod packing, where in the *ac* plane a dense arrangement of bpe ligands is observed and in the diagonal direction a sparse arrangement of  $\text{OLZ}^{4-}$  skeletons is shown (Fig. 1b and c). This unique feature results in the solvent-accessible pore along the crystallographic *a*- and *c*-axis, rather than *b* axis. The window both along the *a*- and *c*-axis is about 3.8 Å, while a relatively bigger window along [1 0 1] direction with a size of 3.8 Å × 5.2 Å is observed (Fig. 1d–g). This size is comparable with the kinetic diameter of Xe atoms (4.047 Å), but bigger than that of Kr (3.655 Å), implying potential size-selective separation for Xe and Kr. Moreover, the accessible pore surfaces of ECUT-60 are mainly low polarity aromatic rings, which are particularly desirable for adsorption of Xe with larger polarizability [25,26], relative to Kr. The solvent-accessible volume occupied by solvent molecules that could not be determined to give exact structure due to their serious disorder, estimated by Platon software [28], is 40.4% of the cell volume, suggesting high porosity.

The loss of trapped solvent molecules from ECUT-60, according to the TG analysis, is before 100 °C (Fig. S2a online). The degassed samples were obtained at 100 °C under vacuum for 24 h after the samples were treated by solvent exchange with low-boiling  $\text{CH}_3\text{OH}$ . Both PXRD and single crystal XRD confirmed the maintenance of framework integrality for the degassed samples (Fig. 2). The stability under water and acid/base environment was traced by PXRD and BET tests (Fig. 2 and Fig. S2b online). Note that the crystals of ECUT-60 render excellent stability in water even after one month (Fig. S3 online). Also, its structure can be well maintained from the acid/base environment at pH 3–12.

The porosity of ECUT-60 was initially evaluated by  $\text{N}_2$  adsorption at 77 K, exhibiting a fully reversible type-I isotherm with a BET surface area of 724  $\text{m}^2/\text{g}$  and a uniform pore size around 4.5 Å (Fig. 3a and insert). This value is comparable with that calculated from the structure of ECUT-60. The permanent porosity was further investigated by  $\text{CO}_2$ ,  $\text{C}_2\text{H}_2$ , and  $\text{C}_2\text{H}_4$  adsorption at 298 K (Figs. S4–S6 online). High adsorption capacity for  $\text{CO}_2$ ,  $\text{C}_2\text{H}_2$ ,  $\text{C}_2\text{H}_4$  was observed, giving 64.8, 74.5, and 61.1  $\text{cm}^3/\text{g}$ , respectively at 1 bar (Table S1 online) [29].

The high porosity and desirable aperture encouraged us to further investigate Xe/Kr separations in detail. First, adsorption isotherms of single-component Xe and Kr were collected at 298 and 273 K (Fig. S7 online). The maximal adsorption capacity decreases along with the increasing temperature, which is a typical character of physical adsorption. The adsorption isotherm of Xe is type I with a steep slope, which is a typical feature of strong adsorbates in microporous materials (Fig. 3b) [29,30], indicating a high affinity of this material towards Xe. By contrast, krypton exhibits very different adsorption behavior, showing almost linear in the whole pressure range. This indicates that krypton is weakly adsorbed by ECUT-60, suggesting a high level of discrimination between Xe over Kr. This can be directly reflected on the adsorption heat enthalpy of Xe and Kr, giving 30 kJ/mol for Xe, significantly higher than the value of 22.6 kJ/mol for Kr (Fig. 3d), suggesting stronger host-guest interactions for Xe than Kr. This can be rationalized on the pore structure in ECUT-60 that is commensurate with Xe (4.047 Å) than Kr (3.655 Å). Of course, the present adsorption heat enthalpy of Xe is lower than the exact matching adsorbent such as the squarate-based MOF showing 43.6 kJ/mol for Xe [26]. But to some extent, this lower adsorption heat enthalpy benefits for material regeneration just with lower energy expenditure.

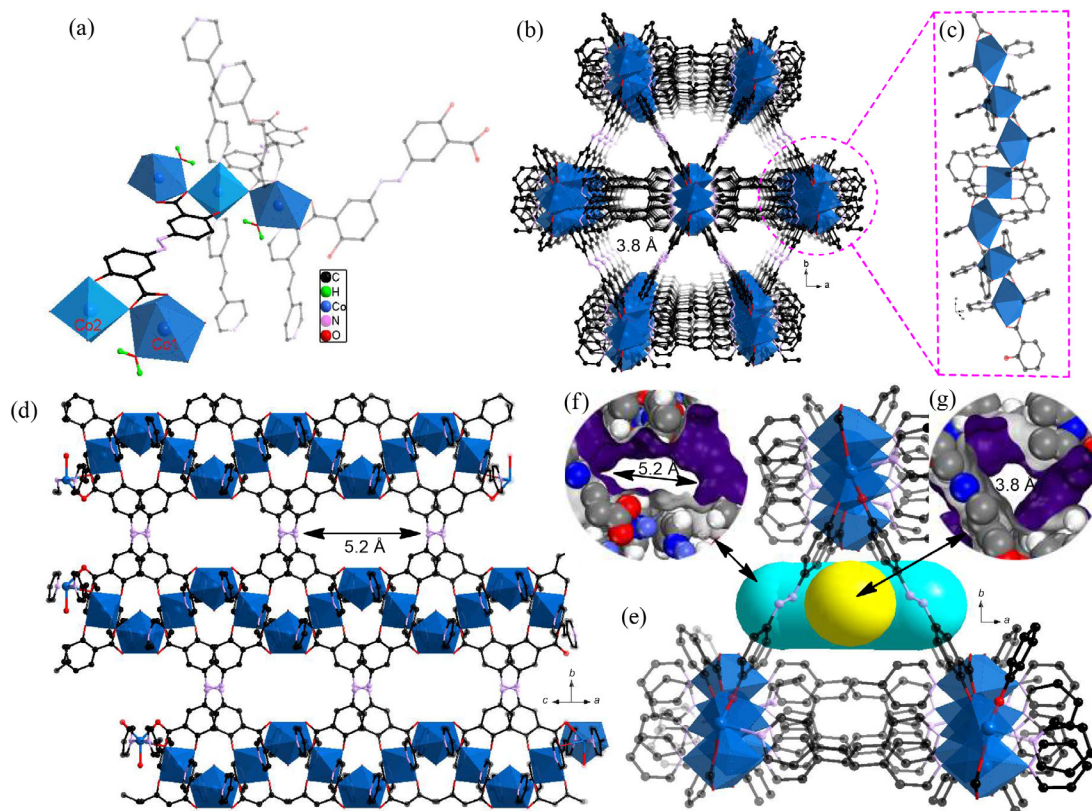


**Fig. 1.** (Color online) The structure of ECUT-60. (a) View of the coordination surrounding around metal ions of Co1 and Co2 sites and their polyhedral geometry, as well as the coordination mode of  $\text{OLZ}^{4-}$  and bpe ligands. The atom code is C/black, H/green, Co/blue, N/purple, O/red. (b) View of the 3D hex-type rod packing built on the rod-like building blocks of vertex-sharing pentagonal bipyramid and octahedron (c). Along  $c$  axis a trigonal window with size of 3.8 Å was observed. (d) Along [101] direction a big ellipse window with size of 3.8 Å × 5.2 Å. (e) A schematic description of the pore along  $c$  axis (yellow section) and [101] direction (cyan section). (f), (g) View of the pore surface and conformation of the ellipse pore along [101] direction and the trigonal pore along  $c$  axis.

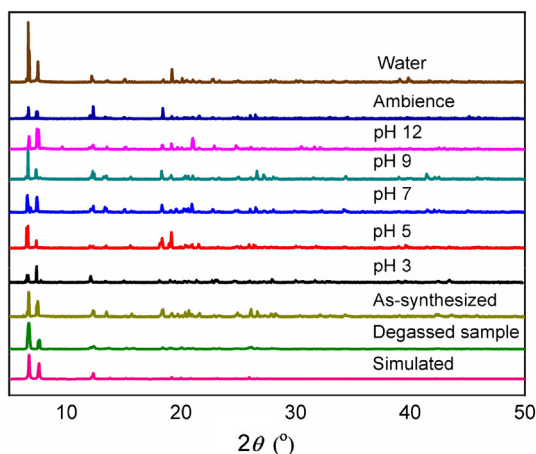


**Fig. 2.** (Color online) The PXRD patterns involved in this work, including in the data simulated from the single crystal data, the as-synthesized samples, the degassed samples, and the samples after exposing in ambience (relative humidity about 70%) for six months or immersing in water for one month, or immersing in water with pH 3–12.

At room temperature and 1 bar, ECUT-60 affords ultrahigh Xe adsorption capacity up to 4.3 mmol/g. This value exceeds most top-performance porous adsorbents [18–26] (Table S2 online) such as  $[\text{Co}_3(\text{HCOO})_6]$  [23], Ni-MOF-74 [27], SB-MOF-1 [25], SB-MOF-2 [22], PAF-45S [32], MOF-Cu-H [33], CROFOUR-1-Ni [34], ZU-62 [18], and the squarate-based MOF (Fig. 3c) [26]. Correspondingly, the Kr adsorption capacity at the same conditions is

1.45 mmol/g, just about one third of that for Xe. Accordingly, highly selective adsorption of Xe over Kr is suggested.

To estimate the adsorption selectivity, we employed the ideal adsorption solution theory (IAST) [18–26] to analyze the experimental isotherm data. The results indicate a high selectivity of 11.36 for a 20/80 binary gas mixtures at room temperature and 1 bar (Fig. S8 online). Such value is comparable with the reported top-performing materials such as  $\text{Co}_3(\text{HCOO})_6$  [23], SB-MOF-1 [25], SB-MOF-2 [22], MOF-Cu-H [32], and CROFOUR-2-Ni [34]. Taking both adsorption capacity and selectivity into consideration, as shown in Fig. S9 (online), ECUT-60 locates at the top, showing an ideal trade in adsorption capacity and selectivity among all reported porous materials. For example, the squarate-based MOF shows the highest selectivity of 69.7 but low adsorption capacity of 1.34 mmol/g [26], while Co-MOF-74 [35] shows the highest adsorption capacity up to 6.1 mmol/g but very low selectivity of 3.91.

Moreover, to predict their capture and separation performances of Xe at dilute condition, we further carried out the calculation of Henry's constants at low pressure (Fig. S9 online) [26,33], giving 22.0 mmol/(g bar), suggesting high affinity of ECUT-60 towards Xe. The corresponding Henry's selectivity is estimated to be 11.6 [26,33], comparable with the result from IAST. Seen from Table S3 (online), it is clear that ECUT-60 shows bigger Henry's constants and selectivity than most porous materials at dilute condition [25].

Based on the above results, we first evaluate the Xe/Kr separation performance of ECUT-60 through simulating the column adsorption processes via transient breakthrough simulations [30,31] on a Xe/Kr (20:80 v:v) mixture. The results show very long

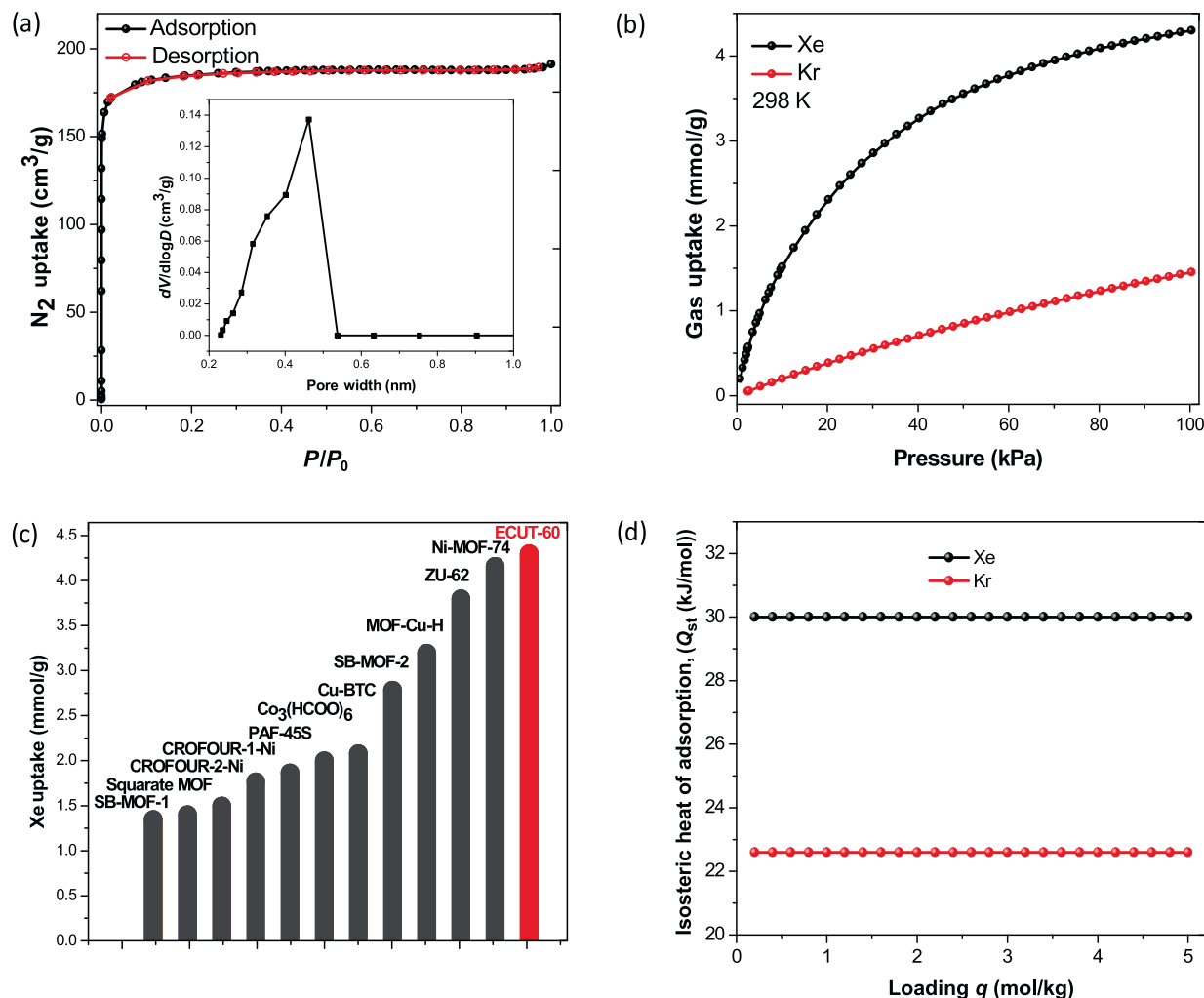


**Fig. 3.** (Color online) The porosity and Xe/Kr adsorption research. (a) The  $N_2$  adsorption at 77 K with the insert of the distribution of pore size. (b) The Xe and Kr uptake at 298 K. (c) A comparison among reported porous materials in the aspect of Xe capture at room temperature. (d) The adsorption heat enthalpy of Xe and Kr, calculated from the single-component Xe and Kr adsorption data at 298 and 273 K.

time interval  $\Delta\tau$  to produce pure product gas of Kr, suggesting excellent Xe/Kr separation performance (Fig. S10 online). To further get its practical separation ability, the dynamic breakthrough experiments at 298 K were carried out for a 20:80 (v:v) Xe/Kr mixture. As shown in Fig. 4, a clean Xe/Kr separation was observed for this mixture, comparable with the transient breakthrough simulations (Fig. S10 online). Kr broke through ECUT-60 bed immediately after 5 min/g, whereas Xe was retained in the column for > 53 min/g. Accordingly, we can collect high-purity Kr (>99.9%) from the outlet effluent with yield of 96 mL/g (Fig. S11 online). At the same time, Xe adsorption capacity is estimated to be 2.25 mmol/g (Fig. S11 online), well consistent with the saturated adsorption capacity from the single-component Xe adsorption isotherms (2.33 mmol/g at 0.2 bar), farly exceeding all reported MOFs at room temperature [18–26], for example MOF-Cu-H (2.05 mmol/g) [33] and CROFOUR-2-Ni (1.91 mmol/g) [34] (Fig. 4c). Interestingly, due to the lower adsorption heat enthalpy for Xe and Kr, the desorption of Xe and Kr can be very easily implemented through 5 mL/min  $N_2$  purge (Fig. 4b and Fig. S11 online), consequently leading to the production of high-purity Xe (>99.9%) of 1.06 mmol/g (approximately 50% of all adsorbed Xe). Moreover, the adsorption–desorption cycle was repeated six times through breakthrough cycle tests (Fig. 4d and Figs. S12, S13 online), without

obvious decrease in the production of Kr and Xe, suggesting the excellent recyclability of ECUT-60 for Xe/Kr separation.

We next explored its application for separation of trace Xe/Kr from a simulated UNF off-gas with a content of 400 ppm Xe, 40 ppm Kr, 78.1%  $N_2$ , 20.9%  $O_2$ , 0.03%  $CO_2$  and 0.9% Ar [26,33]. First, the single-component  $CO_2$ ,  $N_2$ , and  $O_2$  adsorption was measured, giving the uptake of 2.89, 0.25, 0.25 mmol/g, respectively, far below than Xe uptake of 4.3 mmol/g, implying high Xe selectivity (Figs. S14–S16 online). The adsorption heat enthalpy of  $CO_2$ ,  $N_2$  and  $O_2$  was 27.1 kJ/mol, 20.2 kJ/mol, and 20.5 kJ/mol (Figs. S14–S16 online), respectively, at the onset adsorption, smaller than the corresponding value for Xe, implying stronger affinity for Xe than others like that of Kr,  $CO_2$ ,  $O_2$ , and  $N_2$ . The selectivity via IAST calculation (1:99 v:v) at 1 bar is 3.48 for Xe/ $CO_2$ , 113 for Xe/ $N_2$ , and 107 for Xe/ $O_2$  (Fig. S17 online). In this regard, big potential for direct separation of trace Xe/Kr from UNF off-gas can be expected for ECUT-60. Fig. 5 shows the clean separation of Xe from Kr,  $CO_2$ ,  $N_2$ ,  $O_2$ , and Ar at 298 K for a mixture containing 400 ppm Xe, 40 ppm Kr, 78.1%  $N_2$ , 20.9%  $O_2$ , 0.03%  $CO_2$ , and 0.9% Ar. All components except for Xe broke through the column immediately, whereas Xe enables long retention time up to 49 min/g (Fig. 5a). Under these conditions, the Xe adsorption capacity is 70.4 mmol/kg, far exceeding all reported values [35,36] including in SBMOF-1

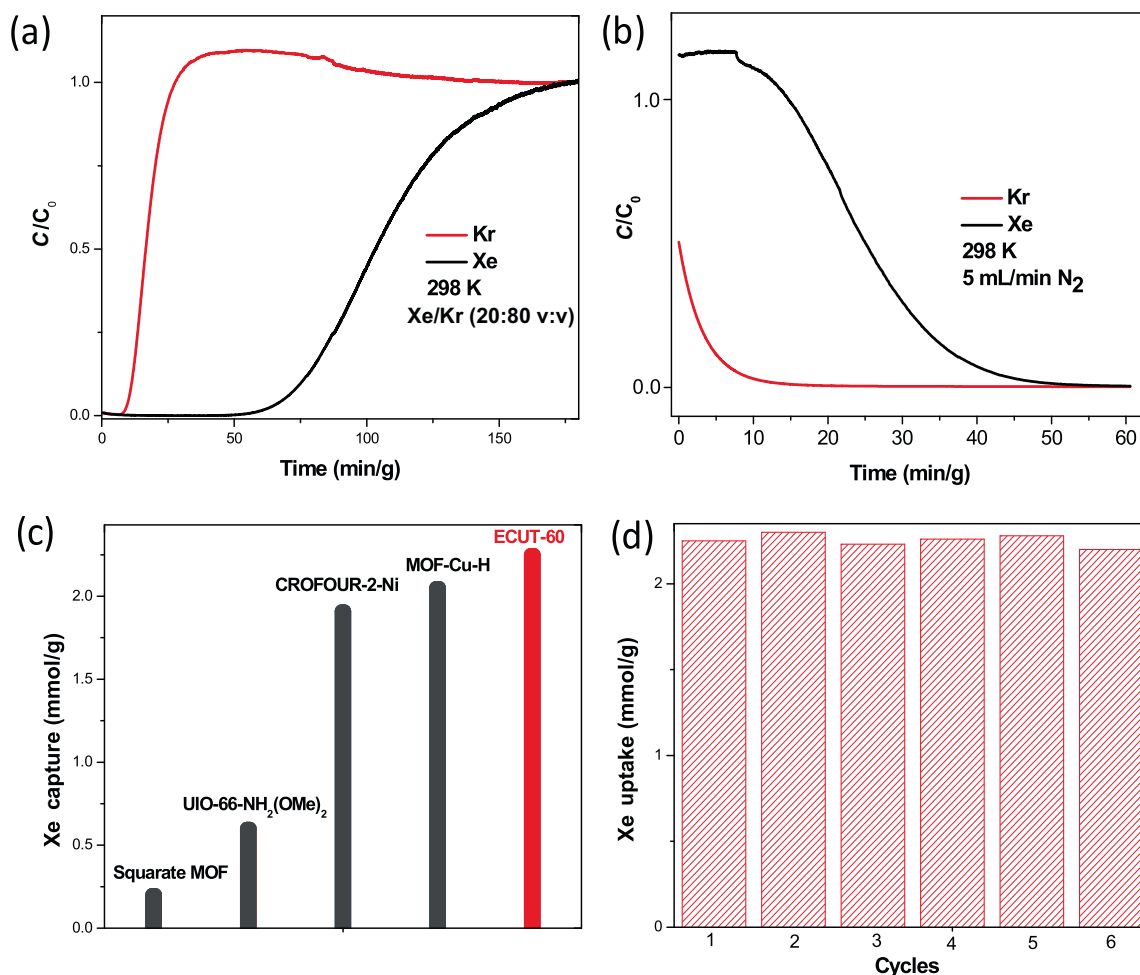


**Fig. 4.** (Color online) The Xe/Kr separation research. (a) Experimental breakthrough curves upon ECUT-60 column for Xe/Kr (20:80 v:v) mixture at 298 K with gas flow of 2 mL/min. (b) The desorption of Xe and Kr and production of Xe under 5 mL/min flow of N<sub>2</sub> at 298 K. (c) A comparison among the reported top-performing MOF materials and our case in the Xe capture aspect under breakthrough manner at room temperature. (d) The 6-times repeated Xe uptake through cycling breakthrough tests.

(13.2 mmol/kg) [25], CC3 (11 mmol/kg) [10], and Ni-MOF-74 (4.8 mmol/kg) [27], creating the record value until now (Fig. 5b and Table S4 online). Similarly, via 5 mL/min N<sub>2</sub> purge the Xe production is up to 19.7 mmol/kg (approximately 30% of all adsorbed Xe, Fig. 5c). To the best of our knowledge, this work should represent the first one with direct production of Xe from simulated UNF off-gas. Remarkably, a 94.2% maintenance in the Xe adsorption capacity (66.3 mmol/kg) was observed for ECUT-60 even in the presence of water vapor (Fig. 5d and Fig. S18 online). This strongly suggests its superior application for direct Xe/Kr separation plus production of pure Xe from UNF off-gas.

To disclose the Xe/Kr separation mechanism in this work, we further carried out the theoretical calculation by GCMC and DFT-D [38]. We initially simulated the Xe, Kr, CO<sub>2</sub>, N<sub>2</sub>, and O<sub>2</sub> adsorption by GCMC (Fig. S19 online). And the calculated results agree well with the experimental data. The density distributions of Xe are mainly located around the pore wall (Fig. S20 online). To exactly disclose the adsorption site for Xe, DFT-D calculation was further performed (Fig. S21 online). Three dominating adsorption sites were observed with binding energy of -46.05 kJ/mol (site I), -40.93 kJ/mol (site II), and -45.53 kJ/mol (site III), far exceeding corresponding value for Kr (-26.97, -29.15, and -22.52 kJ/mol), suggesting stronger affinity towards Xe over Kr. A deep insight into the structure disclosed that all the sites were tightly trapped by atoms on the pore wall (Fig. 6). For site I, the Xe atoms were trapped by eight atoms involved in two carboxylate atoms and six aromatic ring hydrogen atoms in an approximately sandwich

geometry with X-H/O distance of 3.17–3.91 Å. In site II Xe atom was also trapped by one carboxylate atom, one azobenzene nitrogen atom, and six aromatic ring hydrogen atoms with X-H/O/N distance of 2.95–4.04 Å. As for site III, Xe atom was trapped by one carboxylate atom plus five aromatic ring hydrogen atoms with X-H/O distance of 3.11–3.81 Å. Based on the above results, we can conclude that the highly selective adsorption of Xe in ECUT-60 is due to the multiple traps that provide unique affinity towards Xe via van der Waals force and consequently lead to easy regeneration of the material in a low-cost and energy-saving manner.

#### 4. Conclusion

In summary, we present herein a robust MOF with narrow window but high porosity, which allows this material to render not only highly selective adsorption of Xe but also ultrahigh Xe adsorption capacity. Taking both selectivity and adsorption capacity into account, our MOF should be one of the best materials for Xe/Kr separation. At room temperature, the MOF enables remarkable Xe uptake capacity through breakthrough process, exceeding all reported MOFs. Further tests disclosed our MOF as benchmark material for trace Xe/Kr separation, giving a record Xe adsorption capacity up to 70.4 mmol/kg from a simulated UNF off-gas, almost 5.3-fold of SBMOF-1, one of the best materials (13.2 mmol/kg). Impressively, ultrahigh Xe production up to 19.7 mmol/kg can be obtained via a low-cost and energy-saving desorption manner.

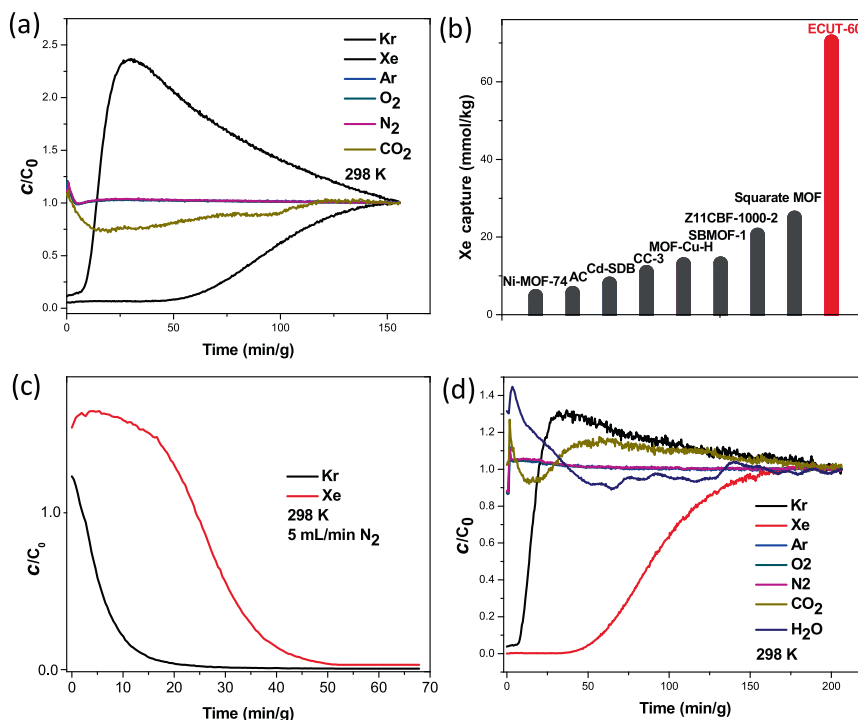


**Fig. 5.** (Color online) The Xe/Kr separation at dilute conditions. (a) Experimental breakthrough curves upon ECUT-60 column for a trace Xe/Kr mixture with content of 400 ppm Xe ( $4 \times 10^{-4}$  bar), 40 ppm Kr, 78.1% N<sub>2</sub>, 20.9% O<sub>2</sub>, 0.03% CO<sub>2</sub> and 0.9% Ar at 298 K with gas flow of 2 mL/min. (b) A comparison among the reported top-performing MOF materials and our case in the Xe capture aspect under breakthrough manner at room temperature and diluted conditions. (c) The desorption of Xe and Kr and production of Kr under 5 mL/min flow of N<sub>2</sub> at 298 K. (d) Experimental breakthrough curves upon ECUT-60 column for a trace Xe/Kr mixture with content of 400 ppm Xe, 40 ppm Kr, 78.1% N<sub>2</sub>, 20.9% O<sub>2</sub>, 0.03% CO<sub>2</sub> and 0.9% Ar at 298 K with gas flow of 2 mL/min and the presence of vapor. The faster breakthrough of CO<sub>2</sub> than Kr in ECUT-60 column is most possibly due to relatively high content of CO<sub>2</sub>, in contrast to Kr; similar trends were often encountered in the literature [12].

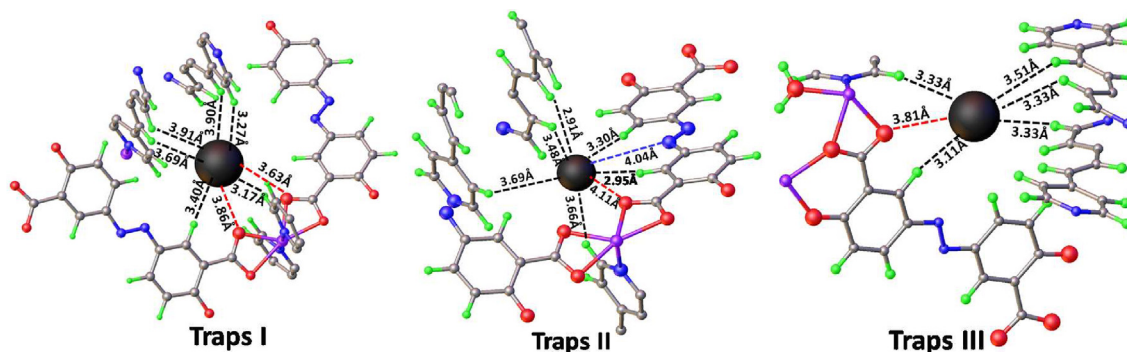


**Fig. 6.** (Color online) DFT-D calculated Xe adsorption binding sites located at three types of traps in ECUT-60. Color code: Co/purple, C/gray, H/green, N/blue, O/red, Xe/black.

More importantly, we also observed the maintenance of high-performance Xe uptake through breakthrough process even under moist environment. Taking the above results in conjunction with the high water, chemical, and thermal stability into consideration, our MOF could be an ideal material for direct separation of Xe/Kr and production of Xe from trace Xe/Kr mixture such as air or UNF off-gas.

#### Conflict of interest

The authors declare that they have no conflict of interest.

#### Acknowledgments

This work was supported by the National Natural Science Foundations of China (21966002 and 21871047), the Natural Science Foundation of Jiangxi Province (20181ACB20003), the Training

Program for Academic and Technical Leaders of Major Disciplines in Jiangxi Province (20194BCJ22010), and the Graduate Innovation Project of East China University of Technology (DHYC-202023).

#### Author contributions

Feng Luo coordinated and conceived the project. Huiping Zhang and Yaling Fan designed and performed the experiments. Feng Luo, Rajamani Krishna, and Xuefeng Feng wrote and finalized the contents of the manuscript. Rajamani Krishna and Li Wang performed data analysis. Rajamani Krishna polished the English language. All authors read and approved the final contents of the study.

#### Appendix A. Supplementary materials

Supplementary materials to this article can be found online at <https://doi.org/10.1016/j.scib.2020.12.031>.

## References

- [1] Kerry FG. Industrial gas handbook: gas separation and purification. Boca Raton, Florida: CRC Press; 2007.
- [2] Nandanwar SU, Coldsnow K, Utgikar V, et al. Capture of harmful radioactive contaminants from off-gas stream using porous solid sorbents for clean environment—a review. *Chem Eng J* 2016;306:369–81.
- [3] Lane G, Nahrwald M, Tait A, et al. Anesthetics as teratogens: nitrous oxide is fetotoxic, xenon is not. *Science* 1980;210:899–901.
- [4] Fontaine J-P, Pointurier F, Blanchard X, et al. Atmospheric xenon radioactive isotope monitoring. *J Environ Radioact* 2004;72:129–35.
- [5] Soelberg NR, Garn TG, Greenhalgh MR, et al. Radioactive iodine and krypton control for nuclear fuel reprocessing facilities. *Sci Technol Nucl Install* 2013;2013:1–12.
- [6] Chen L, Reiss PS, Chong SY, et al. Separation of rare gases and chiral molecules by selective binding in porous organic cages. *Nat Mater* 2014;13:954–60.
- [7] Ullah S, Akram B, Ali H, et al. 2-Methylimidazole assisted ultrafast synthesis of carboxylate-based metal–organic framework nano-structures in aqueous medium at room temperature. *Sci Bull* 2019;64:1103–9.
- [8] Li Y, Huang J, Mo Z-W, et al. Multistep evolution from a metal–organic framework to ultrathin nanosheets. *Sci Bull* 2019;64:964–7.
- [9] Easun TL, Moreau F, Yan Y, et al. Structural and dynamic studies of substrate binding in porous metal–organic frameworks. *Chem Soc Rev* 2017;46:239–74.
- [10] Zhou D-D, Chen P, Wang C, et al. Intermediate-sized molecular sieving of styrene from larger and smaller analogues. *Nat Mater* 2019;18:994–8.
- [11] Islamoglu T, Goswami S, Li Z, et al. Postsynthetic tuning of metal–organic frameworks for targeted applications. *Acc Chem Res* 2017;50:805–13.
- [12] Tao Y, Fan Y, Xu Z, et al. Boosting selective adsorption of Xe over Kr by double-accessible open-metal site in metal–organic framework: experimental and theoretical research. *Inorg Chem* 2020;59:11793–800.
- [13] Wu Y-P, Zhou W, Zhao J, et al. Surfactant-assisted phase-selective synthesis of new cobalt MOFs and their efficient electrocatalytic hydrogen evolution reaction. *Angew Chem Int Ed* 2017;56:13001–5.
- [14] Wang H, Lustig WP, Li J. Sensing and capture of toxic and hazardous gases and vapors by metal–organic frameworks. *Chem Soc Rev* 2018;47:4729–56.
- [15] Tchalala MR, Bhatt PM, Chappanda KN, et al. Fluorinated MOF platform for selective removal and sensing of SO<sub>2</sub> from flue gas and air. *Nat Commun* 2019;10:1328.
- [16] Jaramillo DE, Reed DA, Jiang HZH, et al. Selective nitrogen adsorption via backbonding in a metal–organic framework with exposed vanadium sites. *Nat Mater* 2020;19:517–21.
- [17] Peng Y-L, Pham T, Li P, et al. Robust ultramicroporous metal–organic frameworks with benchmark affinity for acetylene. *Angew Chem Int Ed* 2018;57:10971–5.
- [18] Wang Q, Ke T, Yang L, et al. Separation of Xe from Kr with record selectivity and productivity in anion-pillared ultramicroporous materials by inverse size-sieving. *Angew Chem Int Ed* 2020;59:3423–8.
- [19] Banerjee D, Cairns AJ, Liu J, et al. Potential of metal–organic frameworks for separation of xenon and krypton. *Acc Chem Res* 2015;48:211–9.
- [20] Banerjee D, Simon CM, Elsaïdi SK, et al. Xenon gas separation and storage using metal–organic frameworks. *Chem* 2018;4:466–94.
- [21] Fernandez CA, Liu J, Thallapally PK, et al. Switching Kr/Xe selectivity with temperature in a metal–organic framework. *J Am Chem Soc* 2012;134:9046–9.
- [22] Chen X, Plonka AM, Banerjee D, et al. Direct observation of Xe and Kr adsorption in a Xe-selective microporous metal–organic framework. *J Am Chem Soc* 2015;137:7007–10.
- [23] Wang H, Yao K, Zhang Z, et al. The first example of commensurate adsorption of atomic gas in a MOF and effective separation of xenon from other noble gases. *Chem Sci* 2014;5:620–4.
- [24] Wang Y, Liu W, Bai Z, et al. Employing an unsaturated Th<sup>4+</sup> site in a porous thorium-organic framework for Kr/Xe uptake and separation. *Angew Chem Int Ed* 2018;57:5783–7.
- [25] Banerjee D, Simon CM, Plonka AM, et al. Metal–organic framework with optimally selective xenon adsorption and separation. *Nat Commun* 2016;7:11831.
- [26] Li L, Guo L, Zhang Z, et al. A robust squarate-based metal–organic framework demonstrates record-high affinity and selectivity for Xenon over Krypton. *J Am Chem Soc* 2019;141:9358–64.
- [27] Liu J, Thallapally PK, Strachan D. Metal–organic frameworks for removal of Xe and Kr from nuclear fuel reprocessing plants. *Langmuir* 2012;28:11584–9.
- [28] Spek AL. PLATON SQUEEZE: a tool for the calculation of the disordered solvent contribution to the calculated structure factors. *Acta Cryst* 2015;71:9–18.
- [29] Zhao X, Wang Y, Li D-S, et al. Metal–organic frameworks for separation. *Adv Mater* 2018;30:1705189.
- [30] Xu Z, Xiong X, Xiong J, et al. A robust Th-azole framework for highly efficient purification of C<sub>2</sub>H<sub>4</sub> from a C<sub>2</sub>H<sub>4</sub>/C<sub>2</sub>H<sub>2</sub>/C<sub>2</sub>H<sub>6</sub> mixture. *Nat Commun* 2020;11:3163.
- [31] Luo F, Yan C, Dang L, et al. UTSA-74: a MOF-74 isomer with two accessible binding sites per metal center for highly selective gas separation. *J Am Chem Soc* 2016;138:5678–84.
- [32] Li J, Huang L, Zou X, et al. Porous organic materials with ultra-small pores and sulfonic functionality for xenon capture with exceptional selectivity. *J Mater Chem A* 2018;6:11163–8.
- [33] Xiong S, Gong Y, Hu S, et al. A microporous metal–organic framework with commensurate adsorption and highly selective separation of xenon. *J Mater Chem A* 2018;6:4752–8.
- [34] Mohamed MH, Elsaïdi SK, Pham T, et al. Hybrid ultra-microporous materials for selective xenon adsorption and separation. *Angew Chem Int Ed* 2016;55:8285–9.
- [35] Lee S-J, Kim KC, Yoon T-U, et al. Selective dynamic separation of Xe and Kr in Co-MOF-74 through strong binding strength between Xe atom and unsaturated Co<sup>2+</sup> site. *Microporous Mesoporous Mater* 2016;236:284–91.
- [36] Gong Y, Tang Y, Mao Z, et al. Metal–organic framework derived nanoporous carbons with highly selective adsorption and separation of xenon. *J Mater Chem A* 2018;6:13696–704.
- [37] Banerjee D, Elsaïdi SK, Thallapally PK. Xe adsorption and separation properties of a series of microporous metal–organic frameworks (MOFs) with V-shaped linkers. *J Mater Chem A* 2017;5:16611–5.
- [38] Allen MP, Tildesley DJ. Computer simulation of liquids. Oxford: Clarendon Press; 1987.



Huiping Zhang is a graduate student of Chemistry at East China University of Technology in Prof. Feng Luo's group. He got his M.S. degree in Chemistry from the same group in 2019. His research interest focuses on the synthesis, properties, and application of metal–organic frameworks (MOFs).



Feng Luo received his Ph.D. degree from the Department of Chemistry, Nankai University in 2009, then joined the faculty of School of Biology, Chemistry and Material Science, East China University of Technology, and became a full professor in 2016. His current research interest includes the molecular design and properties of MOFs.

# Robust metal-organic framework with multiple traps for trace Xe/Kr separation

Hui Ping Zhang,<sup>a</sup> Yaling Fan,<sup>a</sup> Rajamani Krishna,<sup>b</sup> Xuefeng Feng,<sup>a</sup> Li Wang,<sup>a</sup> and Feng Luo<sup>a\*</sup>

E-mail: [ecitluofeng@163.com](mailto:ecitluofeng@163.com)

## 1. Experimental Section

**Gas Adsorption Measurements.** Before carrying out the adsorption experiment, the samples of **ECUT-60** was firstly treated by immersing in CH<sub>3</sub>OH for three days to make solvent exchange. Then the samples about 100 mg was degased at 100 °C under vacuum for 24 h in Belsorp-max. The BET was investigated by nitrogen adsorption at 77 K. The single-component isotherms of O<sub>2</sub>, N<sub>2</sub>, CO<sub>2</sub>, C<sub>2</sub>H<sub>2</sub>, and C<sub>2</sub>H<sub>4</sub>, Xe and Kr were collected on the Belsorp-max. The repeat test of Xe adsorption is carried out for the samples after Xe adsorption at 298 K and then exposing in ambience (humidity about 70%) for 24 h. To maintain the experimental temperatures liquid nitrogen (77 K) and temperature-programmed water bath (273 and 298 K) were used respectively.

**Stability test.** Water stability test was carried out by immersing 100 mg samples in water for 30 days. Then PXRD is used to trace the stability. The pH stability test was carried out by immersing 100 mg samples in water with pH=3.0-12 for 2 days. Then PXRD is used to trace the stability.

**X-ray Crystallography.** X-ray diffraction data of **ECUT-60** was collected at 298 K on a Bruker-AXS SMART Breeze CCD diffractometer using graphite monochromated MoK $\alpha$  radiation ( $\lambda=0.71073$  Å). The data reduction included a correction for Lorentz and polarization effects, with an applied multi-scan absorption correction (SADABS). The crystal structure was solved and refined using the SHELXTL program suite. Direct methods yielded all non-hydrogen atoms, which were refined with anisotropic thermal parameters. All hydrogen atom positions were calculated geometrically and were riding on their respective atoms. The SQUEEZE subroutine of the PLATON software suite was used to remove the scattering from the highly disordered guest molecules. A



summary of crystal data is given in Table S5. CCDC 1952310 contains the supplementary crystallographic data of **ECUT-60**. For the degassed samples and the samples after immersing in water for one month, the unit cell is determined as follows,  $a=14.27(2)$  Å,  $b=25.35(4)$  Å,  $c=14.12(2)$  Å,  $\beta=117.58(2)^\circ$ , or  $a=14.671(2)$  Å,  $b=25.940(4)$  Å,  $c=14.301(2)$  Å,  $\beta=118.012(9)^\circ$ , respectively, which is well consistent with the single crystal data for the as-synthesized samples. The data can be obtained free of charge from the Cambridge Crystallographic Data Centre via [www.ccdc.cam.ac.uk/data\\_request/cif](http://www.ccdc.cam.ac.uk/data_request/cif).

**Grand Canonical Monte Carlo (GCMC) simulations.** The GCMC simulations, which were performed by Sorption code[1] in Materiel Studio of Accelrys (MS), were carried out to investigate on the adsorbed capacity of MOF for Xe/Kr at 298 K from 0.001 to 100 kPa. A simulation box of  $1 \times 1 \times 1$  crystallographic unit cell was used. During the simulations,  $5 \times 10^6$  steps were performed to guarantee the equilibration and to sample the desired properties, respectively. Rigid framework assumption was used in all simulations. The universal force field (UFF) [2] was used to describe the interactions, the van der Waals interaction with a cutoff of 23.5 Å were depicted by Lenard Jones 12-6 potential.

**DFT-D calculations.** DFT-D calculations were performed to provide the optimized structures and energies of Xe, Kr, CO<sub>2</sub>, O<sub>2</sub>, and N<sub>2</sub> interaction with the frameworks of MOF. The Perdew-Burke-Ernzerhof (PBE) function [3] under the generalized gradient approximation (GGA) functional with the double- $\xi$  numerical polarization (DPN) basis set was used by CASTEP program package[4] in MS software. Because of using the whole unit cell too large, the smaller primitive cell was used. The tolerances of energy, gradient, and displacement convergence for optimizations were  $2.0 \times 10^{-5}$  eV/atom, 0.05 eV/Å, and 0.002 Å, respectively. The dispersion correction (DFT-D)[5] was considered into calculations of the single point energy, where the energy cutoff was 400.0 eV, the SCF tolerance was  $2.0 \times 10^{-6}$  eV/atom. The binding energy  $\Delta E_{bind}$  for the adsorbed structures the primitive cell with those gases was calculated by Eq. 1 (Table S6),

$$\Delta E_{bind} = E_{complex} - E_{gas} - E_{MOF} \quad (1)$$

where,  $E_{complex}$ ,  $E_{gas}$ , and  $E_{MOF}$  are the total energies of complex of gas with MOF, Xe, Kr, CO<sub>2</sub>, O<sub>2</sub>, and N<sub>2</sub> gases, and the MOF at the optimized geometries, respectively.

**Breakthrough experiment.** In a typical experiment, 0.7 g of adsorbent (in the column Ø 46 mm×150 mm) was activated at 383 K overnight under vacuum in a separate oven.

After the sample is degassed, the column is backfilled with argon and mounted in the set-up. Before starting each experiment, helium reference gas is flushed through the column and then the gas flow is switched to the desired gas mixture at the same flow rate of 2 ml/min. The gas mixture

downstream the column was monitored using a Hiden mass-spectrometer.

The desorption of the adsorbed Xe and Kr was achieved through 5 ml/min N<sub>2</sub> purge after the breakthrough experiment.

**IAST calculations of adsorption selectivities.** The adsorption selectivity of Xe/Kr (20/80 v/v) in **ECUT-60** was established by using the Ideal Adsorption Solution Theory (IAST). Adsorption selectivity  $S_{Xe/Kr}$  is defined as:

$$S_{Xe/Kr} = \frac{X_{Xe}/X_{Kr}}{y_{Xe}/y_{Kr}}$$

Where  $X_{Xe}$  and  $X_{Kr}$  are the equilibrium adsorption capacity of component Xe and component Kr respectively.  $Y_{Xe}$  and  $Y_{Kr}$  are the molar fractions of component Xe and component Kr in the gas phase. The Xe/CO<sub>2</sub>, Xe/O<sub>2</sub>, and Xe/N<sub>2</sub> selectivity was obtained by similar method. The obtained parameter was listed as follows.

Adsorbates	N <sub>1</sub> <sup>max</sup> (mmol/g)	b <sub>1</sub> (kPa <sup>-1</sup> )	n <sub>1</sub>	N <sub>2</sub> <sup>max</sup> (mmol/g)	b <sub>2</sub> (kPa <sup>-1</sup> )	n <sub>2</sub>	R <sup>2</sup>
Xe	1.22375	0.21534	1.1339	3.81322	0.00802	1.3657	0.99999
Kr	3.43605	8.91E-04	1.1185	1.82765	0.00970	1.0099	0.97879
CO <sub>2</sub>	2.09331	0.02859	1.4731	2.15355	0.00687	0.0929	0.98855
N <sub>2</sub>	0.00894	1.658E-08	4.5518	1.49706	0.00205	1.0214	0.99987
O <sub>2</sub>	0.00894	1.658E-08	4.3537	1.50706	0.00195	0.9960	0.99151

**Isosteric heat of adsorption.** The binding energies of Xe, Kr, O<sub>2</sub>, N<sub>2</sub>, and CO<sub>2</sub> in **ECUT-60** are reflected in the isosteric heat of adsorption, Q<sub>st</sub> defined as

$$Q_{st} = (RT^2) \frac{d \ln P}{dT}$$

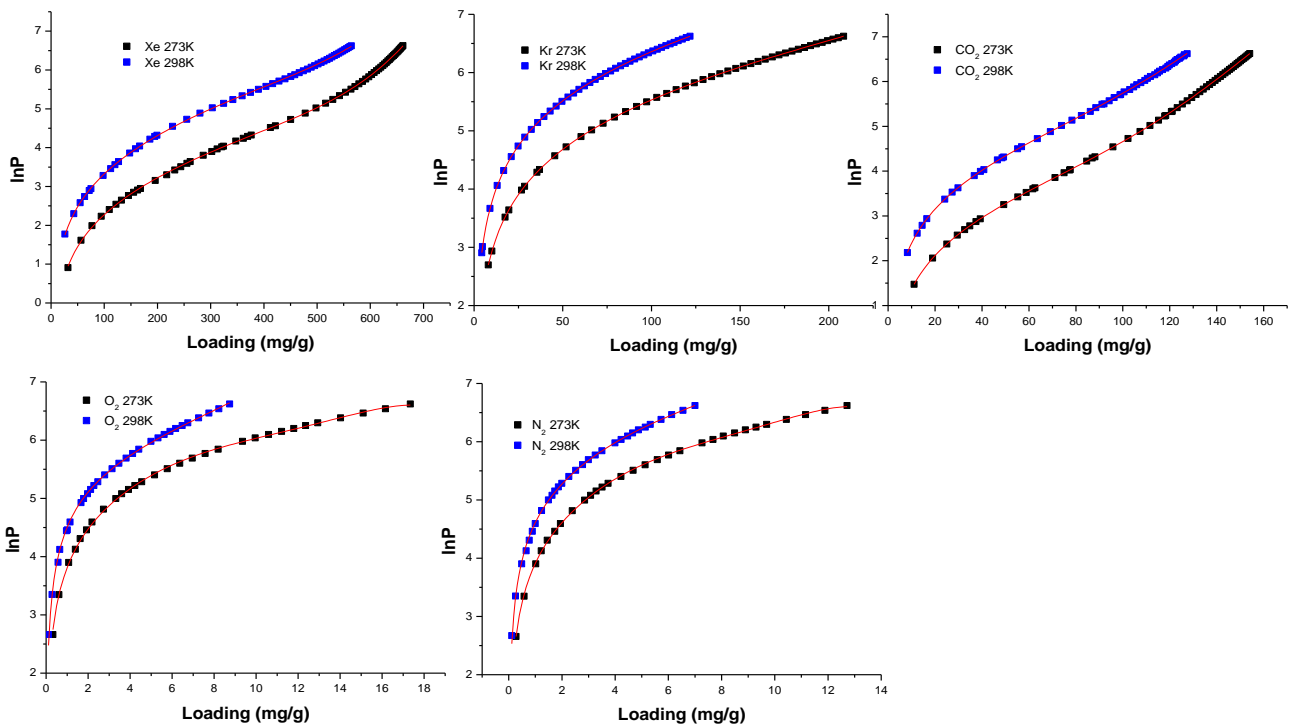
These values were determined by fitting the data at 298 K and 273 K using equation.

$$\ln P = \ln N + \frac{1}{T} \sum_{i=0}^m a_i N^i + \sum_{i=0}^n b_i N^i$$

The obtained parameter was listed as follows.

	Xe	CO <sub>2</sub>	O <sub>2</sub>	Kr	N <sub>2</sub>
--	----	-----------------	----------------	----	----------------

$a_0$	-3616.605	-3277.081	-2491.11	-2760.394	-2442.73
$a_1$	-1.69664	-5.47744	261.7432	1.40736	168.3575
$a_2$	0.00129	0.05193	-20.9537	-0.01239	-6.16691
$a_3$	3.30E-06	-5.97E-04	-1.50438	8.33E-05	-3.67305
$a_4$	-9.45E-09	5.22E-06	0.09464	-3.91E-07	0.31059
$a_5$	1.08E-11	-1.35E-08	-0.00211	7.12E-10	-0.00937
$b_0$	9.36602	11.03206	13.01374	10.69584	12.92525
$b_1$	0.009	0.02222	-1.06847	-4.99E-04	-0.73741
$b_2$	-6.98E-06	-3.19E-05	0.11431	1.42E-05	0.09031
$T_1$	273K	273	273	273	273
$T_2$	298K	298	298	298	298
$R^2$	0.99991	0.99998	0.99858	1	0.99911



**Breakthrough simulations.** The performance of industrial fixed bed adsorbent is influenced by

adsorption selectivity and adsorption capacity. The following parameters were adopted in the breakthrough simulation: the length of the packed bed  $L = 0.3\text{m}$ ; The void ratio of the filling layer is 0.4. Apparent gas velocity at the inlet  $u = 0.04\text{ m/s}$ .

## 2. Characterizations

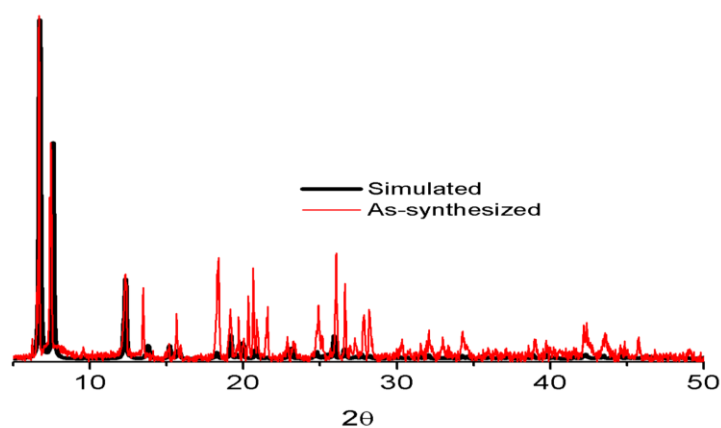


**Fig. S1.** The PXR D patterns simulated from the single crystal data, and derived from the as-synthesized samples.

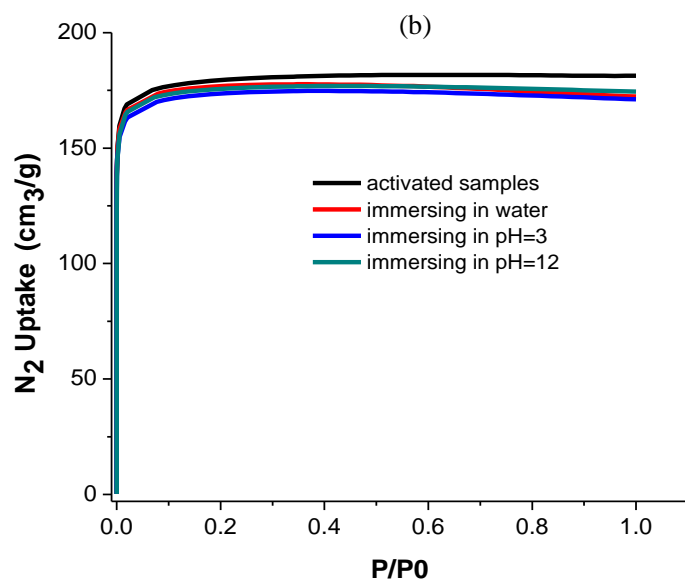
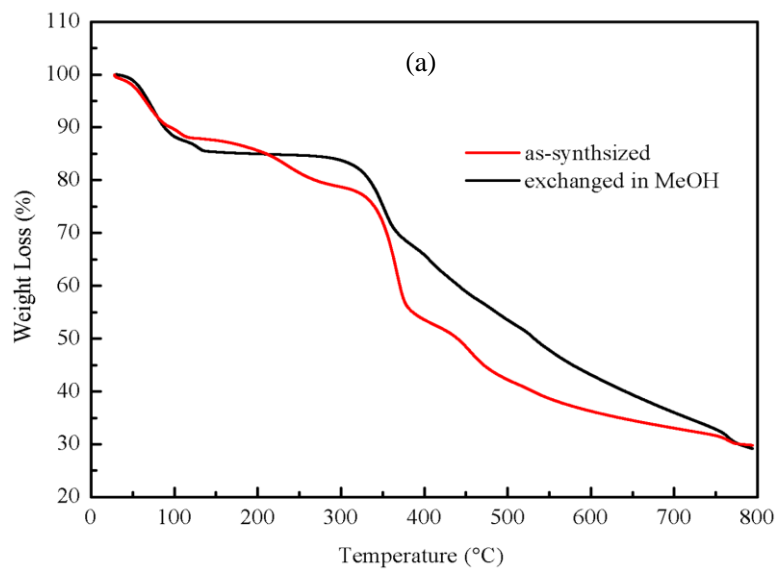


**Fig. S2.** a) The TG plots of the as-synthesized **ECUT-60** samples and the samples after  $\text{CH}_3\text{OH}$  exchange; b) a comparison of BET tests among these samples. The corresponding BET surface area is  $724 \text{ m}^2/\text{g}$  for the activated samples,  $710 \text{ m}^2/\text{g}$  for the samples after immersing in water for one month and then activated,  $708 \text{ m}^2/\text{g}$  for the samples after immersing in  $\text{pH}=3$  solution for one week and then activated,  $707 \text{ m}^2/\text{g}$  for the samples after immersing in  $\text{pH}=12$  solution for one week and then activated.

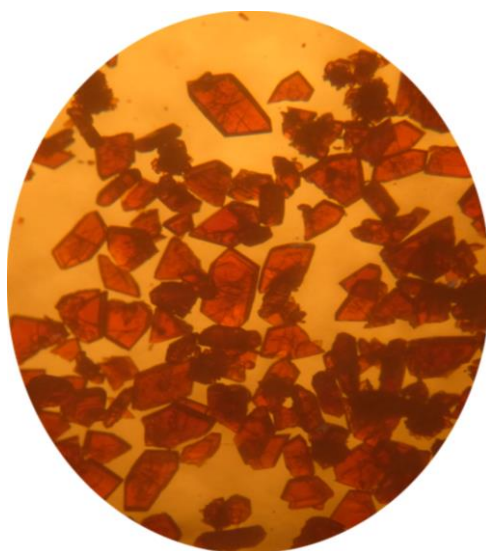


**Fig. S3.** View of the photograph of crystals after immersing in water for 30 days.

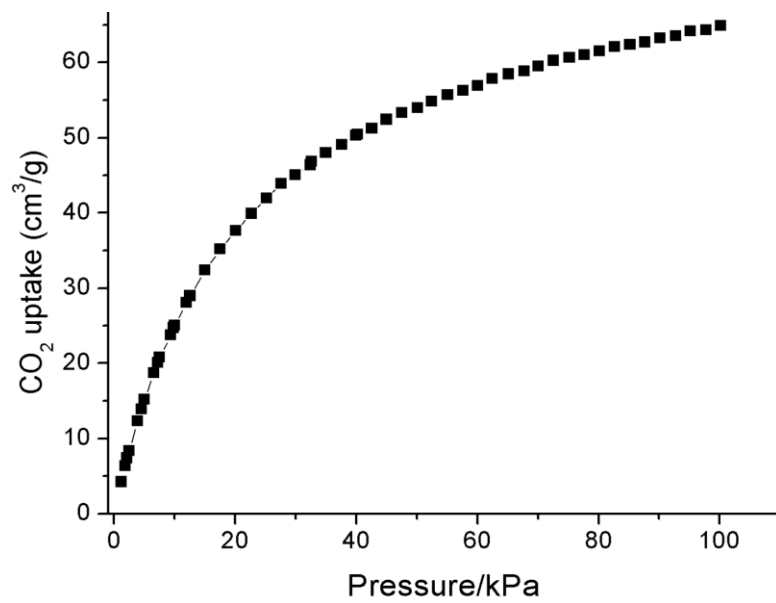


**Fig. S4.** The CO<sub>2</sub> uptake at 298 K.

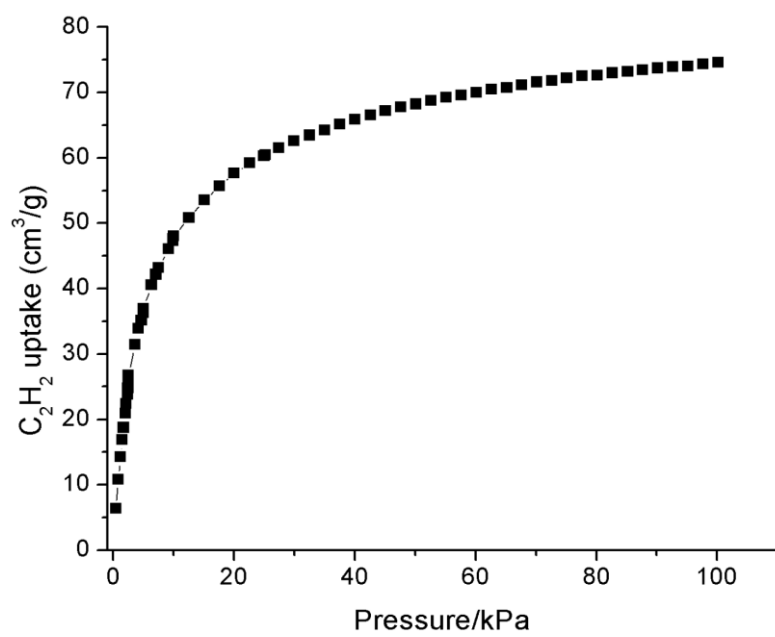


**Fig. S5.** The C<sub>2</sub>H<sub>2</sub> uptake at 298 K.



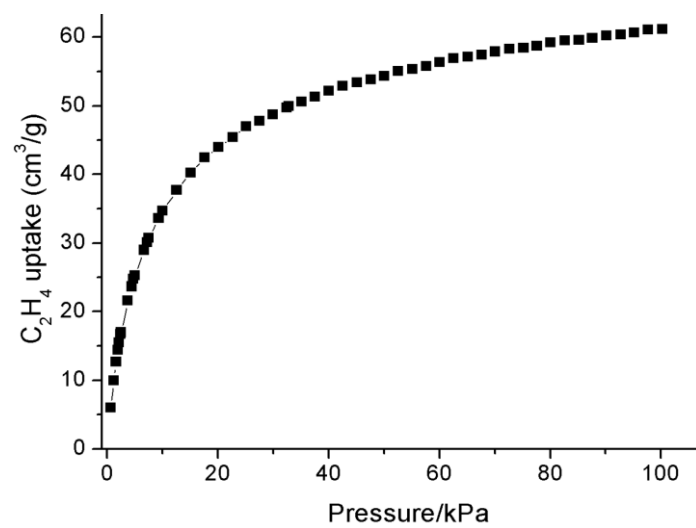


**Fig. S6.** The C<sub>2</sub>H<sub>4</sub> uptake at 298 K.

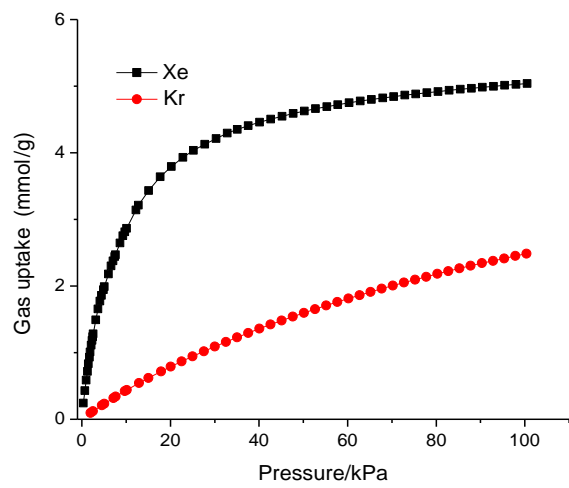


**Fig. S7.** The Xe and Kr uptake at 298k and 273 K.

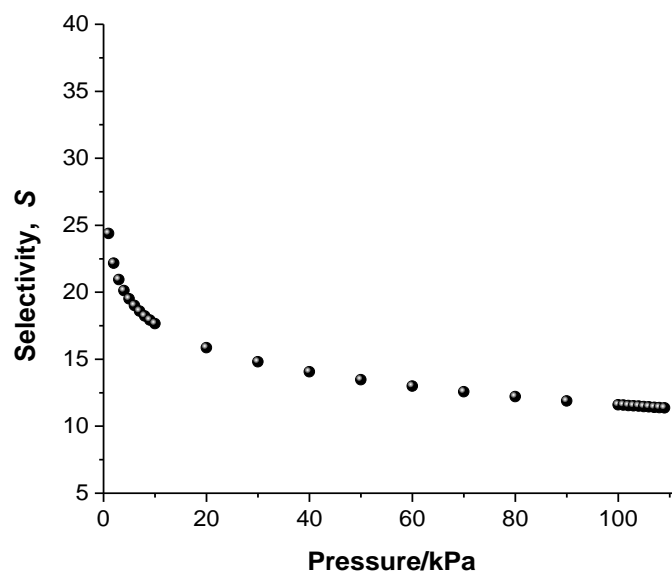


**Fig. S8.** The Xe/Kr selectivity by IAST calculation for 20:80 v/v mixture.

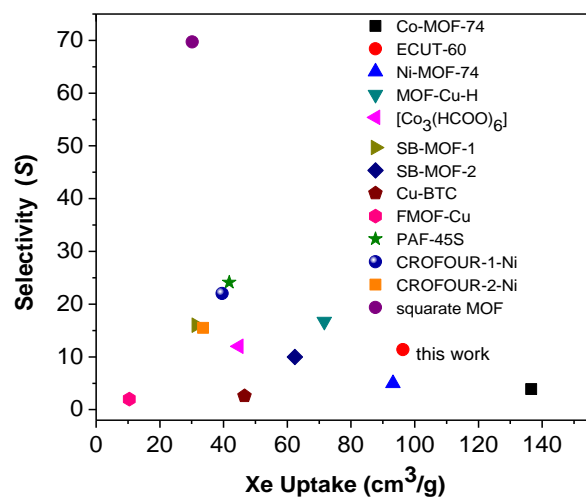


**Fig. S9.** A comparison among all reported top-performing porous adsorbents with our MOF at 1 bar, 298 K with consideration of both adsorption capacity and selectivity.

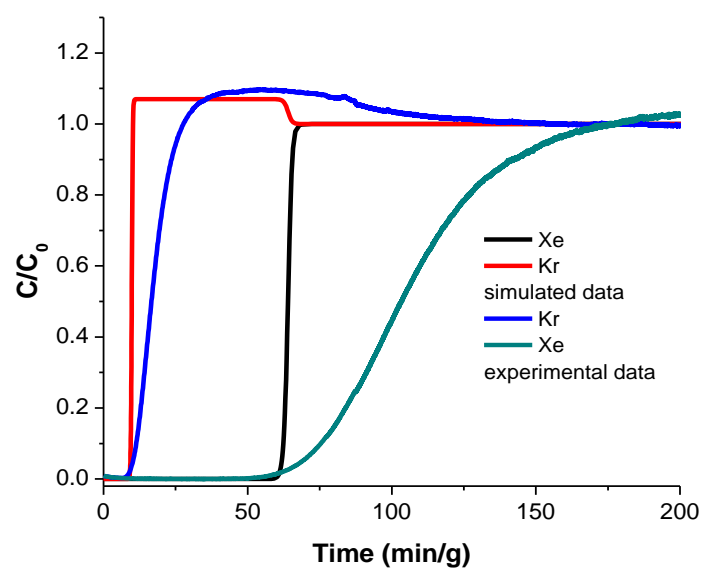


**Fig. S10.** A comparison between the transient breakthrough simulations and the experimental breakthrough on a Xe/Kr (20:80 v/v) mixture at 298 K.

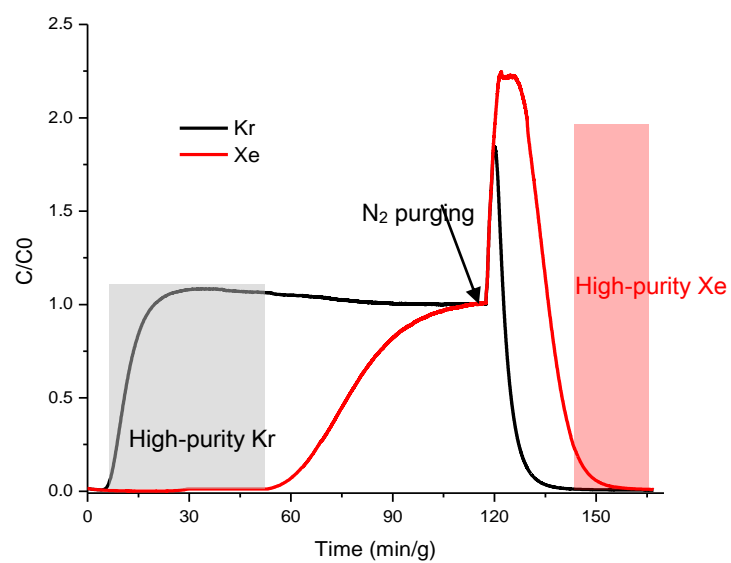


**Fig. S11.** Experimental breakthrough curves upon **ECUT-60** column for the mixture of Xe/Kr (20/80) at 298 K at a total flow of 2 mL/min and following the desorption curves under 5 mL/min flow of N<sub>2</sub> at 298 K.

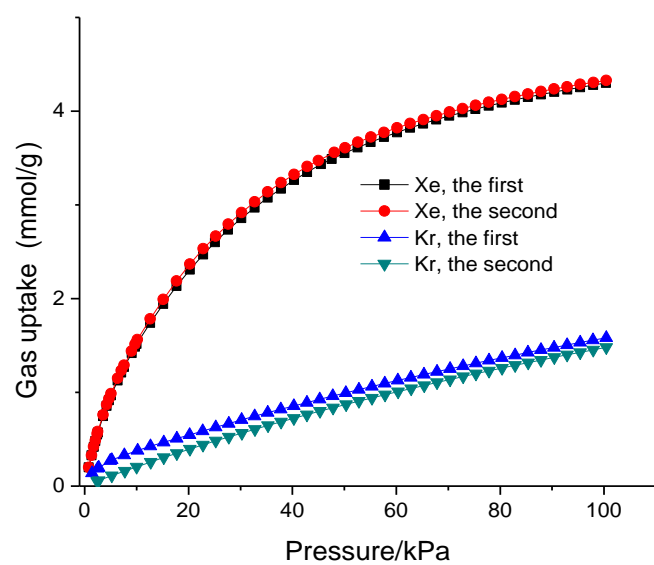


**Fig. S12.** A repeated Xe and Kr adsorption for the first and second time at 298 K.

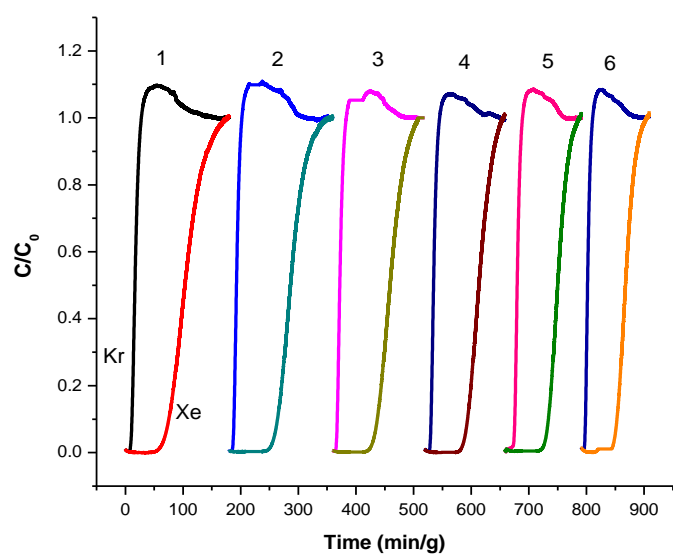


**Fig. S13.** Recycle breakthrough experiments for six times at 298 K.



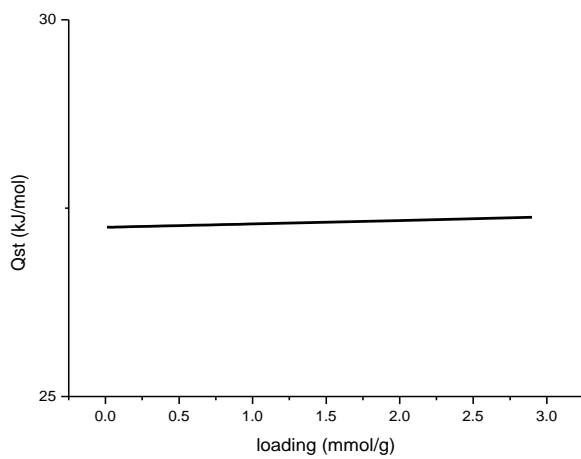
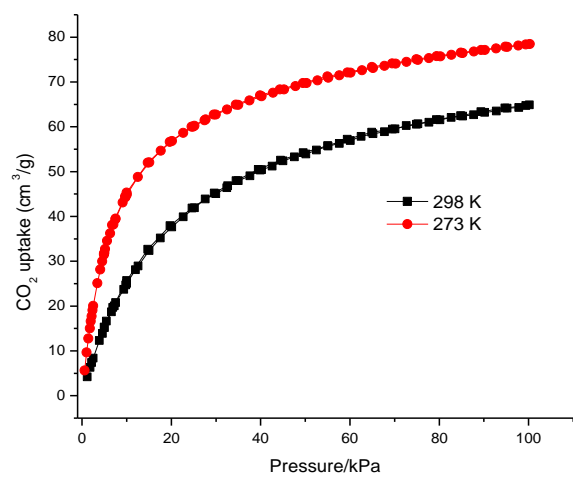


**Fig. S14.** The CO<sub>2</sub> uptake at 298 K and 273 K and the adsorption heat enthalpy of CO<sub>2</sub>.

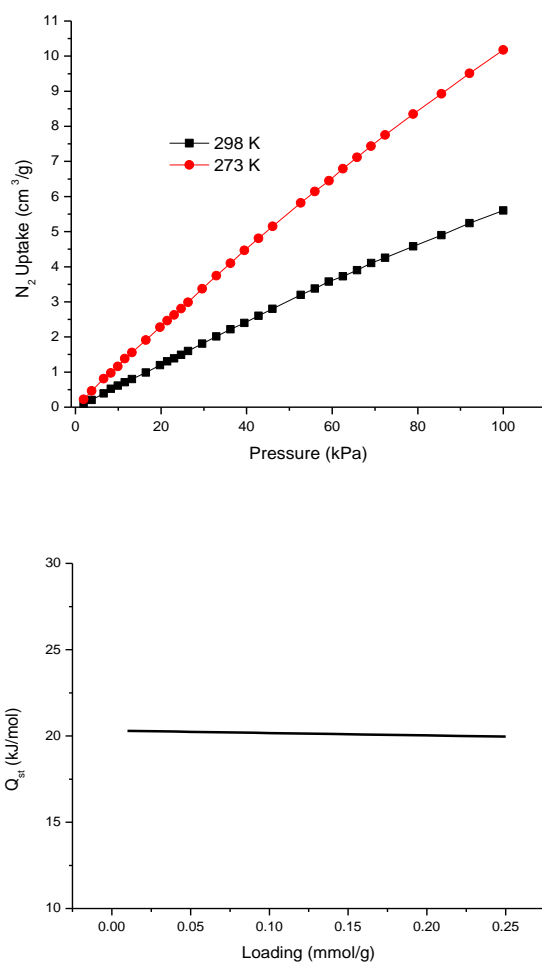


**Fig. S15.** The N<sub>2</sub> uptake at 298 K and 273 K and the adsorption heat enthalpy of N<sub>2</sub>.

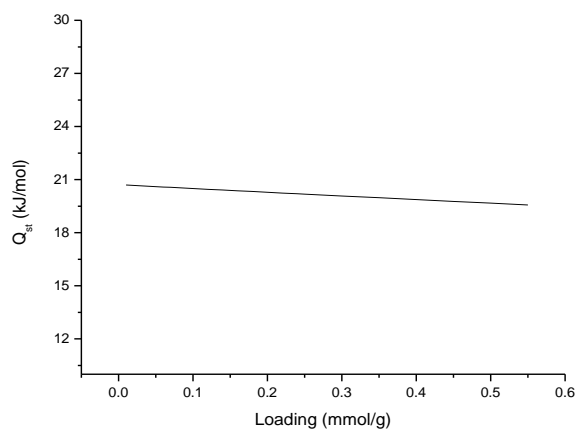
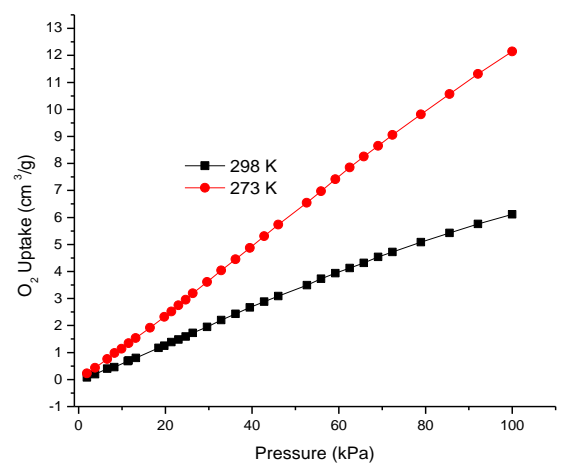


**Fig. S16.** The O<sub>2</sub> uptake at 298 K and 273 K and the adsorption heat enthalpy of O<sub>2</sub>.

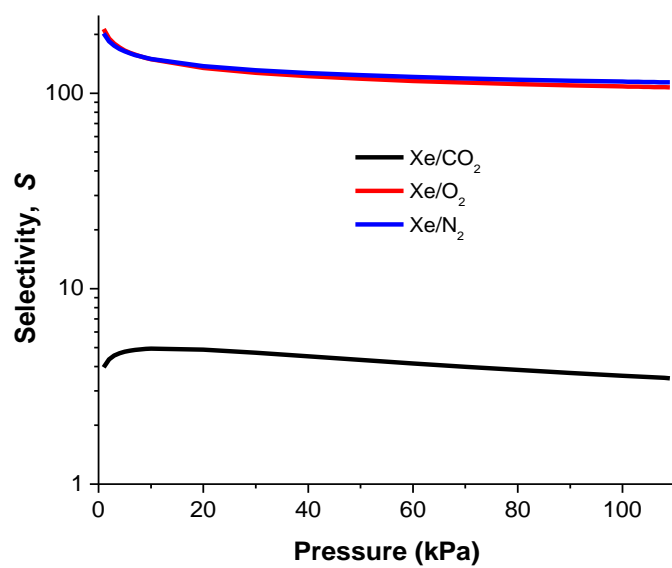


**Fig. S17.** The selectivity of Xe/CO<sub>2</sub>, Xe/O<sub>2</sub>, Xe/N<sub>2</sub> at 298 K for 1:99 v/v mixture.

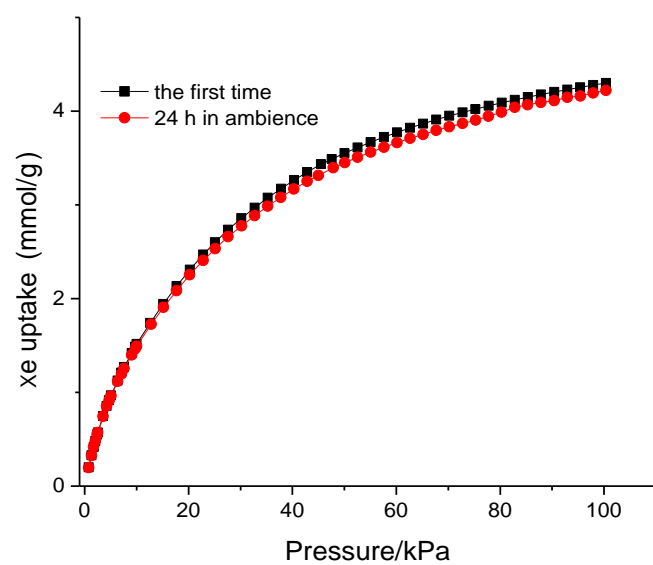


**Fig. S18.** Xe capture upon the activated samples and the counterpart after exposing in ambience for 24 h (humidity of 70%) at 298 K.

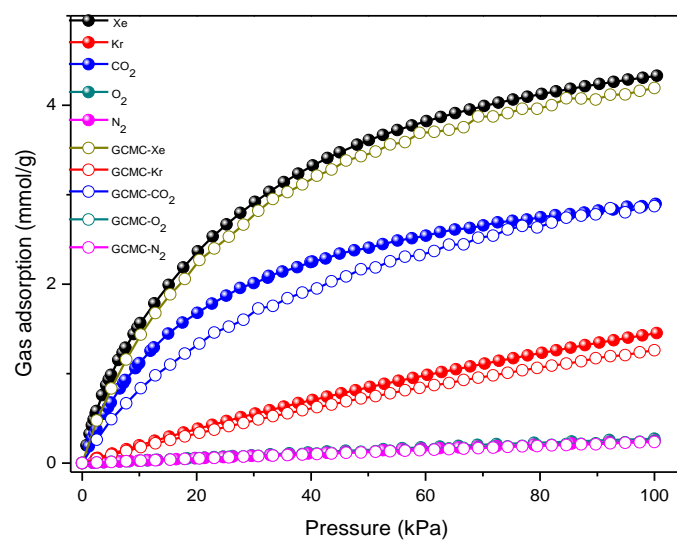


**Fig. S19.** A comparison of experimental and calculated Xe and Kr adsorption by GCMC at 298 K.

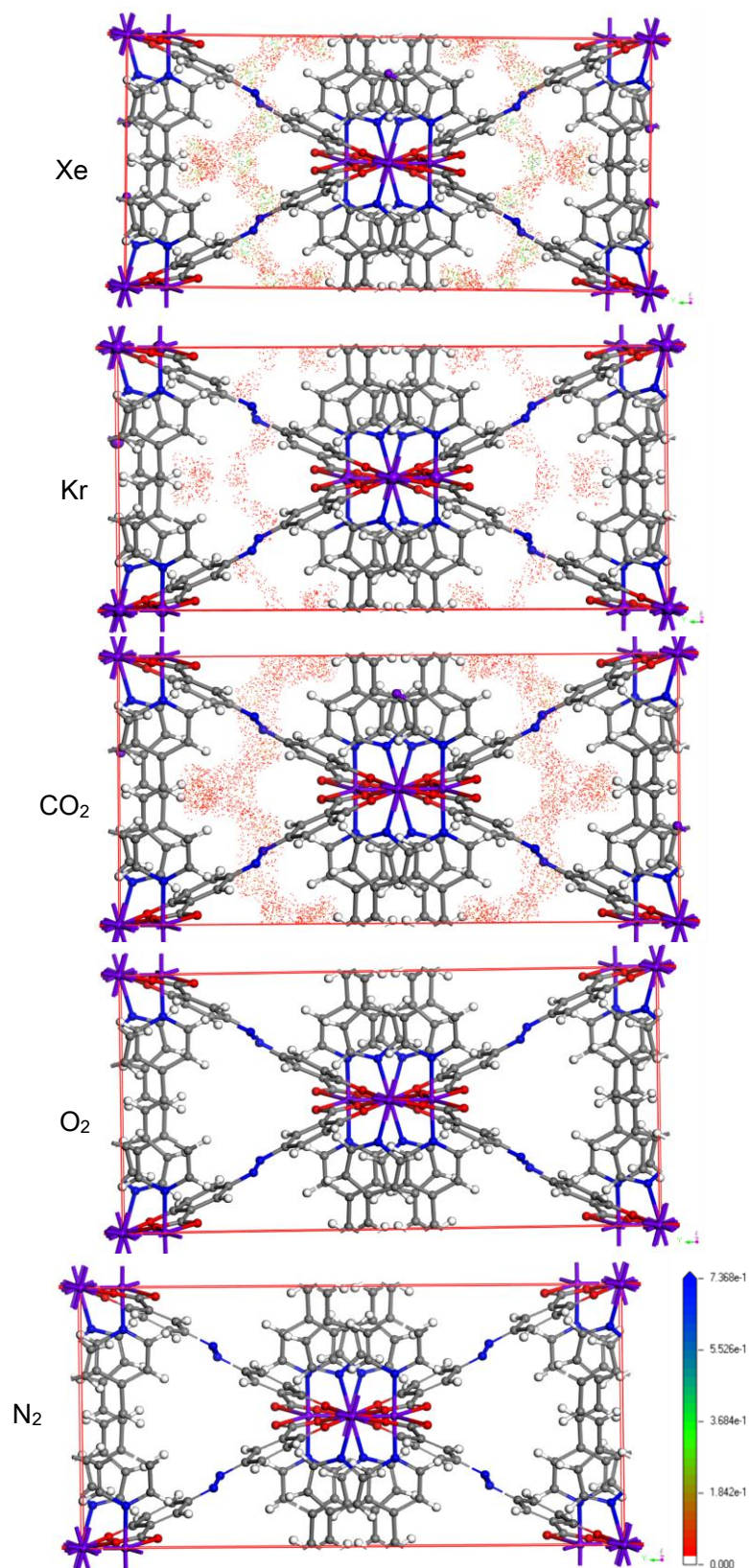


**Fig. S20.** The calculated density distribution of Xe, Kr, CO<sub>2</sub>, O<sub>2</sub>, N<sub>2</sub> in MOF at 298 K at 100 kPa. The ‘color dots’ denoted the size of density distribution.

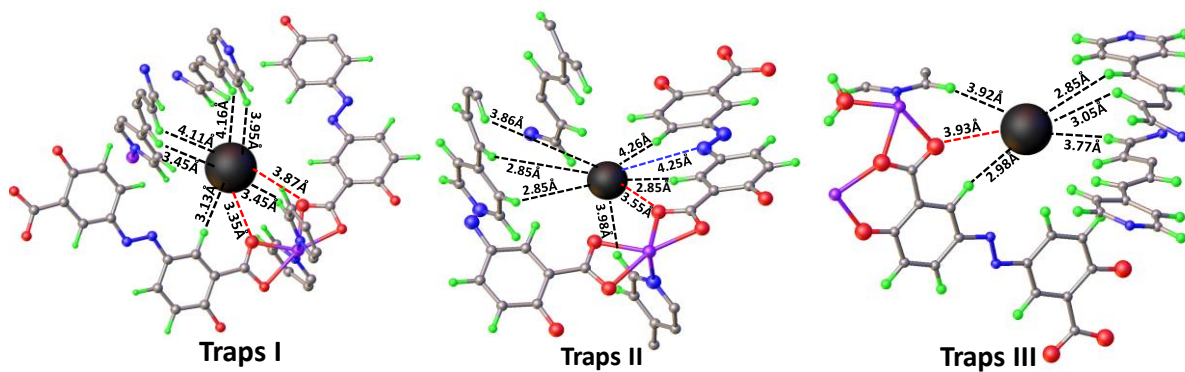


**Fig. S21.** DFT-D calculated Kr adsorption binding sites located at three types of traps in **ECUT-60**. Color code: Co/purple, C/gray, H/green, N/blue, O/red, Xe/black.



**Table S1.** A summary of all gas adsorption data at 298 K and 1 bar for **ECUT-60**.

Type of gas	Adsorption capacity (mmol/g)
Xe	4.3
Kr	1.45
CO <sub>2</sub>	2.89
O <sub>2</sub>	0.27
N <sub>2</sub>	0.25

**Table S2.** A summary of reported porous adsorbents for Xe/Kr separation.

MOF	Xe Uptakes (cm <sup>3</sup> g <sup>-1</sup> )		Xe/Kr Selectivity	Surface area (m <sup>2</sup> /g)	Pore size	References
	0.1 bar	1 bar				
Co-MOF-74	19	136.7	3.91	1346	11 Å	<i>Micropor. Mesopor. Mater.</i> <b>2016</b> , 236, 284-291.
Mg-MOF-74	15	125.44	3.76	1486	11 Å	<i>Micropor. Mesopor. Mater.</i> <b>2016</b> , 236, 284-291.
Ag@MOF-74-Ni	25	103	11.5	749.7	~10 Å	<i>Chem. Commun.</i> <b>2014</b> , 50, 466-468.
Squarate-based MOF	45	56	69.7	95 m <sup>2</sup> /g	4.1 Å×4.3Å	<i>J. Am. Chem. Soc.</i> <b>2019</b> , 141, 9358-64
ZU-62	71.6 (0.2 bar, 273K )	110.8 (273 K)	-	-	5.0 Å	<i>Angew. Chem. Int. Ed.</i> <b>2020</b> , 59, 3423-28
<b>ECUT-60</b>	35	96.31	10.67	724	3.8 Å×5.2 Å	<b>this work</b>
Zn-MOF-74	15	86.9	5.76	1012	11 Å	<i>J. Phys. Chem. C</i> , <b>2014</b> , 118, 11685-11698.
Activated Carbon	28	85	8	778	8 Å	<i>Chem. Comm.</i> <b>2012</b> , 48, 347-349.
Ni-MOF-74	19.32	93.2	7.3	950	11 Å	<i>Micropor. Mesopor. Mater.</i> <b>2016</b> , 236, 284-291.
HKUST-1	-	73.92	8.4	1710	5 Å, 13 Å 11 Å	<i>Micropor. Mesopor. Mater.</i> <b>2013</b> , 169, 176-179.
SIFSIX-3-Ni	20	56.2	-	368	3.66 Å	<i>Chem. Sci.</i> <b>2017</b> , 8, 2373-2380.
SIFSIX-3-fe	7	54.88	-	358	3.5-3.8 Å	<i>Chem. Sci.</i> <b>2017</b> , 8, 2373-2380.
MOF-505	27.87	49.28	8	1030	4.8 Å, 7.1 Å, 9.5 Å	<i>Micropor. Mesopor. Mater.</i> <b>2013</b> , 169, 176-179.
SBMOF-2	18.49	46.14	10	195	6.34 Å, 6.66 Å	<i>J. Am. Chem. Soc.</i> <b>2015</b> , 137, 7007-7010.
[Co <sub>3</sub> (HCOO) <sub>6</sub> ]	18.15	44.78	12	300	5 Å	<i>Chem. Sci.</i> <b>2014</b> , 5, 347-468.
[Ni <sub>3</sub> (HCOO) <sub>6</sub> ]	16.8	39.2	-	331	5-6 Å	<i>Chem. Sci.</i> <b>2014</b> , 5,

						347-468.
[Mn <sub>3</sub> (HCOO) <sub>6</sub> ]	11.2	35.9	-	240	5-6 Å	<i>Chem. Sci.</i> <b>2014</b> , <i>5</i> , 347-468.
MOF-5	8.5	44.35	15	3400	15 Å	<i>Chem. Comm.</i> <b>2012</b> , <i>48</i> , 347-349.
CROFOUR-1-Ni	17.56	40.32	22	505(CO <sub>2</sub> )	-	<i>Angew. Chem. Int. Ed.</i> <b>2016</b> , <i>55</i> , 8285-8289.
CROFOUR-2-Ni	13.38	35.84	15.5	475(CO <sub>2</sub> )	-	<i>Angew. Chem. Int. Ed.</i> <b>2016</b> , <i>55</i> , 8285-8289.
UIO-66	7.8	35.39	3.8	1110	8-11 Å	<i>J. Hazard. Mater.</i> <b>2016</b> , <i>320</i> , 513-520.
SBMOF-1	24.5	31.36	16	145	5.1 Å	<i>Nat. Commun.</i> <b>2016</b> , <i>7</i> , 11831-11837.
FMOF-Zn	3.36	17.92	-	370	5.53 Å	<i>Micropor. Mesopor. Mater.</i> <b>2014</b> , <i>185</i> , 30-50.
FMOF-Cu	1.4	10.8	2	58	5.1 Å × 5.1 Å	<i>Micropor. Mesopor. Mater.</i> <b>2014</b> , <i>185</i> , 30-50.
MIL-101(Cr)	5.64	30.89	4-6	3314	25 Å	<i>J. Hazard. Mater.</i> <b>2016</b> , <i>320</i> , 513-520.
MIL-100(Fe)	2.95	25.5	4-6	1917	8.6 Å	<i>J. Hazard. Mater.</i> <b>2016</b> , <i>320</i> , 513-520.
PAF-45S	14	41.5	24.1	455	5.2 Å,	<i>J. Mater. Chem. A</i> , <b>2018</b> , <i>6</i> , 11163-11168.
PAF-45	10	50	12.3	785.9	5.2 Å	<i>J. Mater. Chem. A</i> , <b>2018</b> , <i>6</i> , 11163-11168.
MOF-Cu-H	46.6	71.6	16.1	868.6	3.7, 4.4 Å	<i>J. Mater. Chem. A</i> , <b>2018</b> , <i>6</i> , 4752-4758.
CC3	20	49.3	20.4	700	4.3 Å	<i>Nat. Mater.</i> <b>2014</b> , <i>13</i> , 954-960.
PCN-14	25	159	6.46	2138	12 Å	<i>J. Phys. Chem. C</i> , <b>2014</b> , <i>118</i> , 11685-1698.
ZIF-8	5.6	28	-	1400	4-4.2 Å	<i>Ind. Eng. Chem. Res.</i> <b>2017</b> , <i>56</i> , 1682-1686.
[Zn(tmz) <sub>2</sub> ]	5.6	67.2	-	710.5	4.3 Å	<i>J. Mater. Chem. A</i> , <b>2015</b> , <i>3</i> , 10747-10752.
NOTT-100	20	136.7	6.89	1619	10.8 Å	<i>J. Phys. Chem. C</i> , <b>2014</b> , <i>118</i> , 116851-1698.
NOTT-101	10	105	5.34	2749	16 Å	<i>J. Phys. Chem. C</i> , <b>2014</b> , <i>118</i> , 11685-11698.

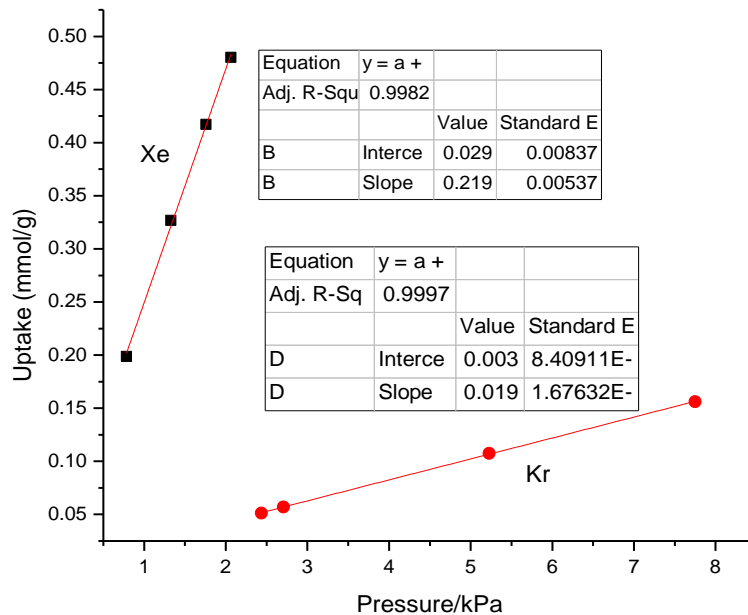
NOTT-102	6.5	55	3.9	2355	16.6 Å	<i>J. Phys. Chem. C</i> , <b>2014</b> , 118, 11685-11698.
NOTT-103	12.5	91.8	5.49	2814	16.2 Å	<i>J. Phys. Chem. C</i> , <b>2014</b> , 118, 11685-11698.
MFU-4l	8	40.3	5	3500	9.1 Å	<i>Micropor. Mesopor. Mater.</i> <b>2012</b> , 162, 64-68.

---

**Table S3.** A comparison of Henry's constants and selectivity among some reported top-performing porous materials and our case.

Compounds	Henry's constants/Xe mol kg <sup>-1</sup> bar <sup>-1</sup>	Henry's constants/Kr mol kg <sup>-1</sup> bar <sup>-1</sup>	Henry's selectivity
FMOF-Cu	0.58	0.43	1.34
IRMOF-1	1.67	0.51	3.27
ZincTetrazolate	1.45	0.38	3.82
Ni-MOF-74	8.4	1.44	5.83
Co-MOF-74	13.5	1.3	10.38
Mg-MOF-74	6.2	1.05	5.9
Zn-MOF-74	4.43	0.77	5.75
PCN-14	8.88	1.5	5.92
MOF-505	10.26	1.52	6.75
HKUST-1	12.19	1.44	8.46
SBMOF-2	10.45	1.21	8.63
Co-formate	9.93	0.93	10.67
CC3	15.51	1.21	12.8
SBMOF-1	38.42	2.37	16.2
Our case	22	1.9	11.6

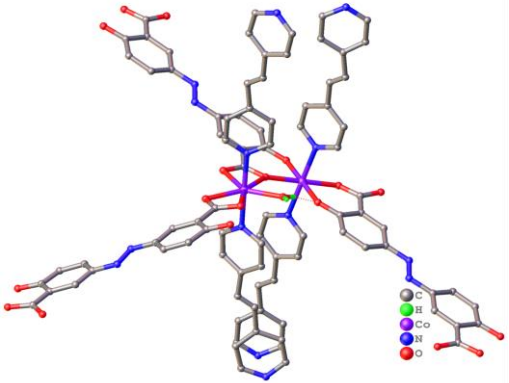
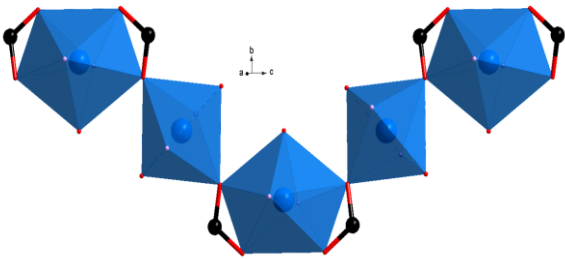
Noted: these values were referenced from ref. 10b. The fitting results of Henry's rule was shown as follows.



**Table S4.** A comparison of Xe adsorption capacity from a simulated UNF reprocessing off-gas system.

<b>Compounds</b>	<b>Xe adsorption capacity (mmol/kg)</b>	<b>References</b>
ECUT-60	70.4	This work
SBMOF-1	13.2	<i>Nat. Commun.</i> <b>2016</b> , 7, 11831
CC3	11	<i>Nat. Mater.</i> <b>2019</b> ,18, 994-98
Ni-MOF-74	4.8	<i>Langmuir</i> <b>2012</b> ,28,11584-89
SBMOF-1	8	<i>J. Mater. Chem. A</i> <b>2017</b> ,5, 16611-15
Squarate-based MOF	25	<i>J. Am. Chem. Soc.</i> <b>2019</b> ,141,9358-64
Z11CBF-1000-2	20.6	<i>J. Mater. Chem. A</i> <b>2018</b> , 6,13696-704

**Table S5.** The crystal parameter of **ECUT-60**.

Complex	<b>ECUT-60</b>
Formula.	$C_{38}H_{28}Co_2N_6O_7$
Formula weight	798.54
Wavelength (Å)	0.71073
Temperature/K	298(2)
Crystal system	Monoclinic
Space group	C2/c
Unit cell dimensions (Å)	a=14.724(8), b=26.295(14), c=14.491(8)
$\beta$	117.889(6) °
volume/Å <sup>3</sup>	4959(5)
Mu (mm <sup>-1</sup> )	0.711
Z	4
Dcalc /g cm <sup>-3</sup>	1.168
F(000)	1632
h, k, l max	17, 31, 17
Nref	4366
Tmin, Tmax	0.931, 0.945
Tmin'	0.931
Data completeness	99.9%
GOF	0.929
Final R indices [I>2sigma(I)]	R <sub>1</sub> =0.064, wR <sub>2</sub> =0.1685
	 <p>The 1D rod-building blocks.</p>
The coordination surrounding around metal ions.	

**Table S6.** The binding energies for MOF with Xe, Kr, CO<sub>2</sub>, O<sub>2</sub>, and N<sub>2</sub> at three regions.

	I region	II region	III region
Xe	-46.05	-40.93	-45.53
Kr	-26.97	-29.15	-22.52
CO <sub>2</sub>		-32.15	
O <sub>2</sub>	-31.51	-28.92	-23.65
N <sub>2</sub>	-28.56	-25.26	-21.65

Noted: the unit is kJ/mol

### *References*

1. Allen MP, Tildesley DJ. Computer Simulation of Liquids. Clarendon Press: Oxford, 1987.
2. Rappé AK, Casewit CJ, Colwell K, et al. UFF, a full periodic table force field for molecular mechanics and molecular dynamics simulations. J. Am. Chem. Soc. 1992;114:10024–10035.
3. Perdew JP, Burke K, Ernzerhof M. Generalized gradient approximation made simple. Phys. Rev. Lett. 1996;77:3865-3868.
4. Clark SJ, Segall MD, Pickard CJ, et al. First principles methods using CASTEP. Zeitschrift fuer Kristallographie 2005;220:567-570.
5. Tkatchenko A, Scheffler M. Accurate molecular van der waals interactions from ground-state electron density and free-atom reference data. Phys. Rev. Lett. 2009;102:073005.